A GALLIUM ARSENIDE CCD X-RAY DETECTOR

By

Scott Patten

B. Sc. (Physics) Simon Fraser University, 1994

A THESIS SUBMITTED IN PARTIAL FULFILLMENT OF

THE REQUIREMENTS FOR THE DEGREE OF

MASTER OF SCIENCE

in

THE FACULTY OF GRADUATE STUDIES

DEPARTMENT OF PHYSICS & ASTRONOMY

We accept this thesis as conforming

to the required standard

THE UNIVERSITY OF BRITISH COLUMBIA

October 1997

In presenting this thesis in partial fulfilment of the requirements for an advanced degree at the University of British Columbia, I agree that the Library shall make it freely available for reference and study. I further agree that permission for extensive copying of this thesis for scholarly purposes may be granted by the head of my department or by his or her representatives. It is understood that copying or publication of this thesis for financial gain shall not be allowed without my written permission.

Department of Physics & Astronomy
The University of British Columbia
6224 Agricultural Road
Vancouver, B.C., Canada
V6T 1Z1

Date: Oct 6, 1997

Abstract

A one dimensional buried channel CCD with a 30 μm thick intrinsic layer was manufactured at TRIUMF for use as a radiation detector. In order to characterize the detector's response to radiation, six discrete X-Ray sources with energies ranging from 8 KeV to 60 keV were impinged on the device. An algorithm was developed to convert events detected by the CCD into spectra characteristic of each X-Ray source. The range of energies detectable and the energy resolution of the detector at different energies were studied.A model was developed and used to explain the shape of each spectrum. The spectrum from an ^{241}Am source was also studied to determine the detector's response to a multi-energetic source.

Table of Contents

List of Tables

List of Figures

Chapter 1

Introduction

1.1 Motivation

The Charge Coupled Device (CCD) was first conceptualized by Boyle and Smith [1] in 1970, and was experimentally verified using Si, in the same year, by Amelio [2]. Since then, CCDs have been used in a large and varied number of applications, with the two major areas being imaging[3, 4, 5, 6] and digital signal processing[7, 8, 9].

Although Si CCDs have been used to detect X-Rays[10, 11, 12] and single element GaAs particle and X-Ray detectors have been built[13, 14, 15], few, if any GaAs CCD detectors have been made. GaAs has advantages over Si because its larger Z value increases the detection efficiency of X-Rays. Also, GaAs device structures are inherently more radiation hard than those made on Si[16, 17]. The mobility of electrons in GaAs is larger than in Si, making GaAs devices potentially faster. Finally, the large band gap of GaAs makes it usable at room temperature, unlike Si and Ge based detectors. These properties would make a GaAs detector useful in many different environments. The detection efficiency of GaAs would make it useful in X-Ray astronomy for detection of X-Rays from 10 – 100 keV[10], while the radiation hardness of GaAs would make these detectors useful in such high particle flux environments as the LHC (Large Hadron Collider)[18].

1.2 Work Done in this Study

The CCDs used in this study were originally used as transient digitizers in the Brookhaven National Laboratories Experiment 787[19]. It was thought that by simply increasing the depth of the epitaxial layer of GaAs on which the CCDs were fabricated, the CCDs would be useful for directly detecting radiation. A wafer of CCDs with a 30 μm thick epitaxial layer was fabricated at the GaAs Micro-structure Laboratory at TRIUMF. The purpose of this study was to find the response of the GaAs CCD detector to X-Rays with energies ranging from 8 to 60 keV. In order to do this, an X-Ray source which emitted the K_α X-Rays of either Cu, Rb, Mo, Ag, Ba or Tb was used. The K_α X-Rays were shone on the CCD and the resulting spectra found. An ^{241}Am source was used as well to study the detector's response to more complex spectra. The spectra from the K_α X-Rays were not single peaks, but instead exhibited a number of features. The features arose from escape of photons and electrons from the detector's volume, noise sources in the detector and deposition of charge in areas of the detector that had little or no drift field. In order to understand these features, several simulations of the microscopic interactions and transport of photons and electrons within the detector were made. Using the results from the simulations, each peak in each individual spectrum was assigned to a phenomenological source. From the positions and widths of the peaks arising from the the deposition of the full energy of a single X-Ray of known energy into the CCD's wells, the energy response and resolution of the GaAs CCD to X-Rays was found.

1.3 Outline

The thesis is divided into seven chapters, the first being the introduction. The second chapter introduces the structure and operation of the CCD. In the third chapter, the interactions of particles in GaAs and the creation of electron hole pairs are discussed.

The fourth chapter details the transport of electrons from their initial creation to the time they enter the potential wells under the CCD gates. The fifth chapter details the experimental work done in this study and shows some of the spectra obtained. The sixth chapter discusses and analyzes the data obtained and shows the results of simulations done to help explain the spectra. The final chapter discusses possible work that could be done in the future and makes conclusions. An appendix shows all of the single energy X-Ray spectra that were taken in this study.

Chapter 2

The CCD

2.1 Overview

Figure 2.1 shows a diagram of a Charge Coupled Device (CCD). It consists of a number of metal contacts, or gates, on top of a semiconductor substrate. Four of the gates act together to form a "pixel". By putting different voltages on the four gates, together with a broad area bias normal to the surface, three dimensional potential wells can be formed where electrons will be trapped. By changing the gate voltages in sequence, charge can be transferred from pixel to pixel. The broad area bias localizes the pixels to the near-surface region and also attracts electrons from the bulk area of the CCD into the pixels.

In normal CCD operation, the voltage on each of the four gates in a pixel consists of a periodic train of pulses with fixed phase with respect to each other. Figure 2.6 shows the voltages on the four gates of a pixel in the CCD used in this study. The effect of these pulse sequences is to move a packet of electron charge from one pixel to the next.

The creation of electron hole pairs (e.h.p.s) in the CCD and their collection under one of the pixels of the CCD is shown in figure 4.10. When an X-Ray enters a CCD, it interacts with the semiconductor substrate of the CCD, creating electron-hole pairs. The number of electron-hole pairs created in the CCD is directly proportional to the energy of the incident X-Ray. The electrons created by the X-Ray are accelerated by the vertical field in the CCD, which drives them into the potential wells under the gates.

The electrons in the potential wells are then transferred from pixel to pixel to the output of the CCD by the gate pulses shown in figure 2.6. The voltage generated at the output when the charge is output from the CCD should therefore provide a measure of the X-Ray's energy.

2.2 The Structure of the CCD

The CCD used in this study (see Figure 2.1) is a buried channel resistive gate CCD comprised of 128 pixels. Each pixel of the CCD consists of four metal gates which are 2 μm wide and spaced by 3 μm, giving a pixel length, or pitch, of 20 μm. The gates are in ohmic contact with a 0.1 μm thick sheet of Cermet (Cr-SiO), a resistive dielectric with a sheet resistance of ~1 M$\Omega/\Box$ at this thickness. The Cermet makes a Schottky contact with the GaAs below it. The Cermet serves two purposes. First, the Schottky barrier moves the potential well away from the surface of the GaAs (see Figure 2.2). This avoids problems associated with trapping of the electrons in the well by the surface states inherent in GaAs. The Cermet also ensures that the voltage between gates varies linearly along the surface of the CCD, providing an electric field that helps in the transfer of electrons from pixel to pixel[20] (see Figure 2.6). The channel of the CCD, the region where the potential wells in the CCD exist, is 50 μm wide and 2.5 mm long (128 pixels $\times$ 20 μm).

Below the gate contacts and the Cermet is a wafer of GaAs. This wafer consists of three layers. On top is an epitaxially grown 0.27 μm thick layer of n-type GaAs doped at $N_D = 5 \times 10^{16}$ cm^{-3}. Below this is a second epitaxially grown, 30 μm thick layer of semi-insulating GaAs, which is p-type with a nominal doping of $N_A < 10^{14}$ cm^{-3}. This layer is called the active layer as this is where the X-Rays interact with the GaAs to form

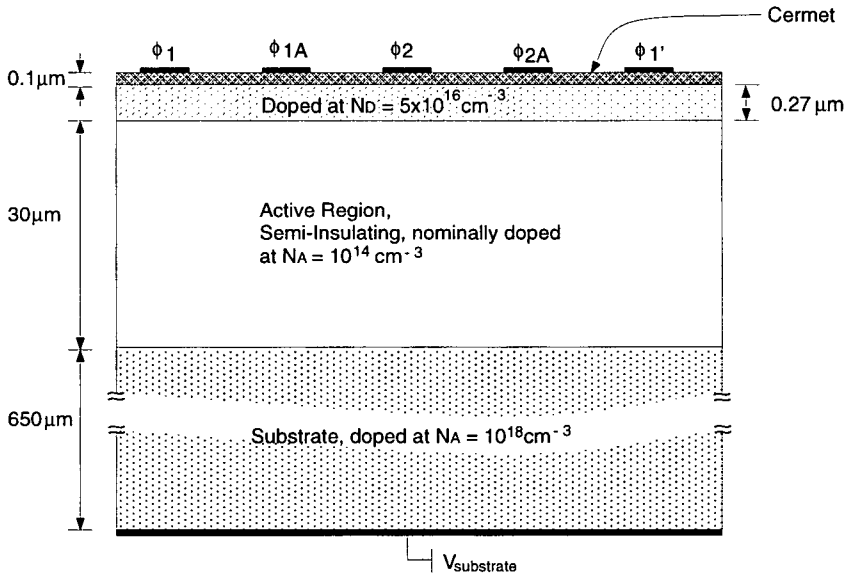

Figure 2.1: A schematic diagram of the CCD used in this study, showing a single pixel.

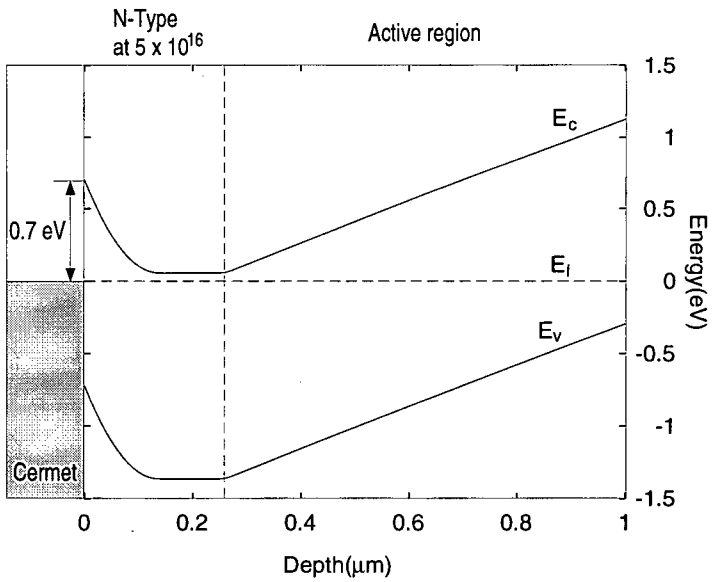

Figure 2.2: The well created under the CCD.

electron-hole pairs (e.h.p.s). Below the epitaxial layers is a 650 μm thick substrate of p-type GaAs grown by the Liquid Encapsulated Czochralski (LEC) method, and doped at $N_A = 10^{18}$ cm^{-3}. The bottom of the CCD has an ohmic contact made to it. This contact is kept at a negative voltage while the CCD is being used as a detector.

2.3 The potential underneath a gate in the CCD

Figure 2.3 shows the band diagram underneath one of the gates in the active area of the CCD with all the gates at ground. The device consists of three junctions, a p^+–p^- junction, a p^-–n junction and a Schottky junction between the n layer and the Cermet. The p^-–n junction and the n–Cermet junction act together to form a potential well with a flat minimum from 0.1 μm to 0.27 μm deep in the CCD. The depletion region is ~4 μm deep, leaving a field-free region 26 μm deep.

When a negative voltage is put on the bottom contact of the device, the p^+–p^- and the p^-–n junctions act as reverse-biased diodes, and the n–Cermet junction acts as a forward biased Schottky diode. To find the depletion depth in the active region under reverse bias conditions, a number of approximations are made. The abrupt junction approximation assumes that the changes in doping are step functions. The second approximation is that there is a well defined depletion region outside of which all fields are zero. The next step is to find how much voltage is dropped across each junction. To do this, a current continuity equation is set-up.

The current density through a pn junction diode[21] or a Schottky diode[22] at a

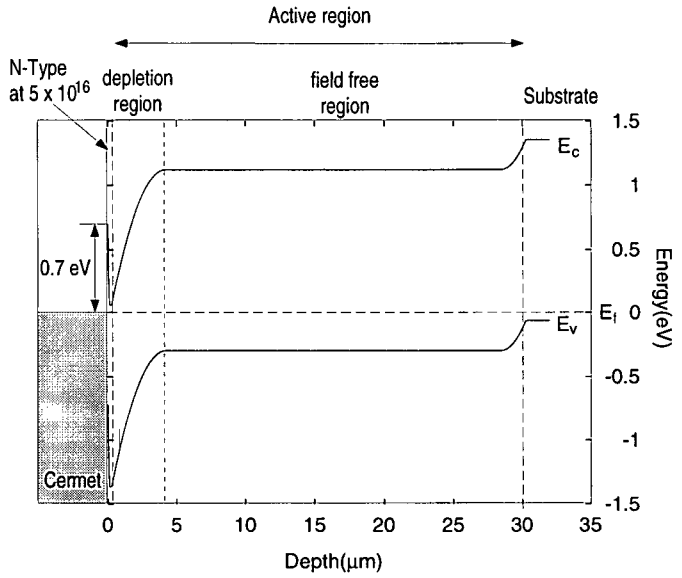

Figure 2.3: The band diagram under a pixel of the CCD with $V_{bias} = 0$ V

temperature T is given by the Schockley equation,

$$J = J_s(e^{qV/k_BT} - 1) \tag{2.1}$$

Where V is the bias voltage across the junction, and is defined to be positive for forward bias and negative for reverse bias. J_s is the saturation current density, and k_B is Boltzmann's constant. For a pn junction, J_s is given by[21]

$$J_s = \frac{qD_p p_{n0}}{L_p} + \frac{qD_n n_{p0}}{L_n} \tag{2.2}$$

Where D_p and D_n are the hole and electron diffusion constants, and L_p and L_p are the hole and electron diffusion lengths, given by

$$L_n = \sqrt{\tau_n D_n}\ ,\ L_p = \sqrt{\tau_p D_p} \tag{2.3}$$

Table 2.1: Constants for GaAs used in calculating the saturation current density in pn and Schottky junctions.[21],[22]

Parameter	Value
D_n	222 cm^2/s
D_p	10.4 cm^2/s
L_n	14.58 μm
L_p	3.16 μm
τ_n	$\sim 10^{-8}$ s
τ_p	$\sim 10^{-8}$ s
n_i	1.79×10^6 cm^{-3}
m^*	0.067 m_0
ϕ_B	0.7 eV

n_{p0} and p_{n0} are the electron and hole minority concentrations on the p and n side of the junction, respectively. They can be found using the fact that the electron and hole density, n and p in a doped semiconductor are related to the intrinsic electron density, n_i by

$$np = n_i^2 \tag{2.4}$$

Table 2.1 gives values for the parameters named in the above equations. The saturation current density has two components added together. The first is linearly dependent on the hole concentration on the n side of the junction, and the second on the electron concentration on the p side of the junction.

For a Schottky diode with a barrier energy of ϕ_B running at a temperature T, the

saturation current density is given by[22]

$$J_s = AT^2 \exp \frac{-\phi_B}{k_B T} \tag{2.5}$$

where A is

$$A = \frac{4\pi m^* q k_B^2}{h^3} \tag{2.6}$$

m^* is the effective mass of an electron in GaAs, $0.067m_0$ (m_0 being the electron mass), and h is Planck's constant.

For the p^-–n junction, $n_{p0} \gg p_{n0}$, so the saturation current for this junction, $J_{s_{pn}}$, will be given by

$$J_{s_{pn}} \approx \frac{qD_n n_{p0}}{L_n} \sim 10^{-14}\mathrm{A/m}^2 \tag{2.7}$$

For the p^+–p^- junction, p_{n0} is given by the doping density in the p^- region, so the saturation current density through this junction, $J_{s_{pp}}$ is

$$J_{s_{pp}} \approx \frac{qD_p p_{n0}}{L_p} \sim 10^{3}\mathrm{A/m}^2 \tag{2.8}$$

For the Schottky junction at 300°K, the saturation current density, $J_{s_{Schottky}}$ is

$$J_{s_{Schottky}} = AT^2 \exp \frac{\phi_B}{k_B T} \sim 10^{-9}\mathrm{A/m}^2 \tag{2.9}$$

The saturation current for the p^-–n junction is much smaller than the saturation current for the other two junctions, so the current through the p^--n junction will be the

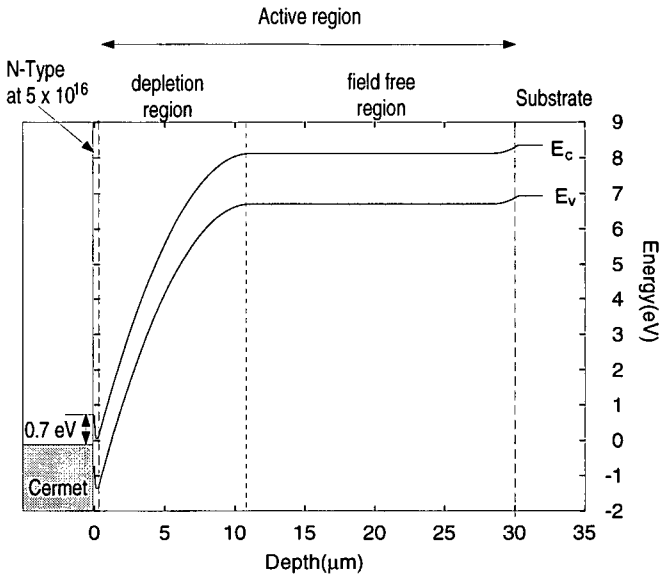

Figure 2.4: The band diagram under a pixel of the CCD with V_{bias} = -7 V

limiting current, and all the applied voltage will be dropped across this junction. Using this information, the band diagram under the CCD was calculated for negative voltages applied to the bottom of the CCD. Figure 2.4 shows the band diagram underneath one of the gates with the voltage at the bottom of the CCD set to -7 V, the voltage used during this study. The depletion width is ~11 μm, leaving a field free region in the active region of 20 μm. The maximum field in the device is 15 kV/cm, much less than the breakdown field of GaAs of 300 kV/cm[21]. The field will vary linearly from zero at the deepest part of the depletion region to 15 kV/cm at the p^-–n junction.

2.4 Movement of charge from pixel to pixel

If the gates in a pixel are named, from left to right, ϕ_1, ϕ_{1A}, ϕ_2 and ϕ_{2A} (see figure 2.1), the voltages on ϕ_1 and ϕ_{2A} are constant, while the voltages on ϕ_2 and ϕ_{1A} change between two levels in synchronism with an input clock signal. In this experiment, the clock signal was run at 10 MHz. ϕ_1 and ϕ_{2A} were set at -0.5V and -1.5V, respectively. The ϕ_2 electrode alternated between 2.5V and -2.5V and the ϕ_{1A} electrode alternated between 0V and -4V. Figure 2.5 shows the signals on the gates of a CCD pixel. Figure 2.6 shows the corresponding electron potential beneath the pixel at four different times in the clock cycle. The figure also shows how a small packet of charge is moved from its original position under ϕ_1 to a position under the ϕ_1 gate of the next pixel to the right. At $t=t_0$, the signal charge is under ϕ_1. At a time t_1, the voltages on ϕ_{1A} and ϕ_2 go positive, and the charge starts to move towards the ϕ_2 electrode. At $t=t_2$, the charge has all moved to the ϕ_2 electrode. At t_3, the voltages on ϕ_{1A} and ϕ_2 go negative, and the charge starts moving towards the ϕ_1 gate of the next pixel, $\phi_{1'}$. The charge has been moved from one pixel to the next. In this study, the CCD was used in the continuous operation mode: the clock signal is constantly input to the CCD, and charge is moved from one pixel to the next at a rate equal to the clock's frequency.

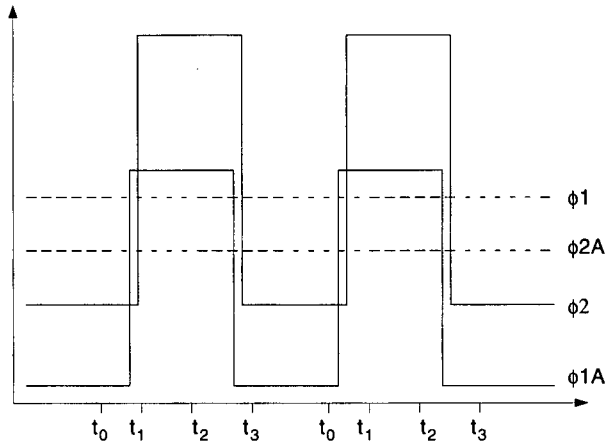

Figure 2.5: The voltages on the phases of a pixel of the CCD

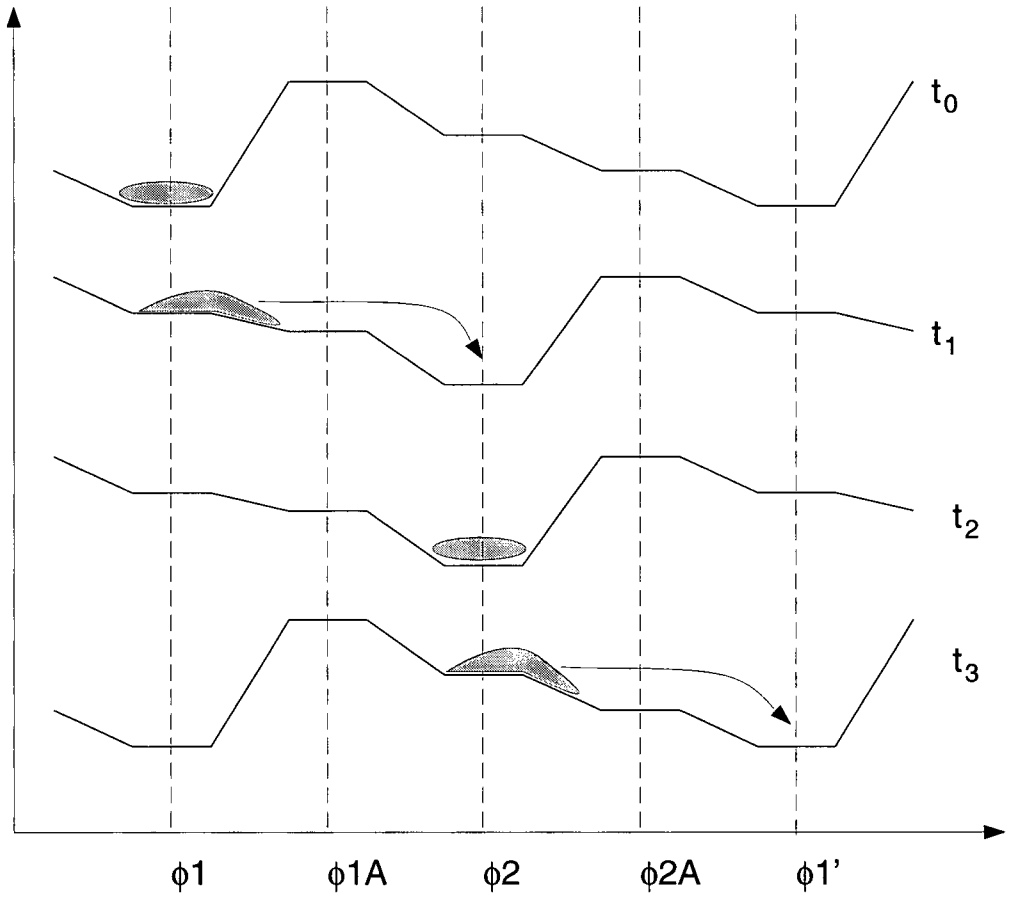

Figure 2.6: A diagram showing the potential along the CCD at times t_0, t_1, t_2 and t_3. An electron "packet" is also shown being transferred from one pixel to the next.

Chapter 3

Interactions of Particles in GaAs

3.1 Introduction

An X-Ray in GaAs will interact with the GaAs by ejecting an energetic electron from one of the atoms through either the Compton or photo-electric process. Both of these processes leave an excited atom, which will relax to its ground state by either emitting a secondary X-Ray or, through an Auger process, an energetic electron. If a secondary X-Ray is released, it will then interact with another atom, liberating another electron. This will result in two energetic electrons (with energies from 10 to 50 keV) in the GaAs. These electrons, as they move through the crystal, will interact with the Ga and As atoms to create further electron-hole pairs. The electrons will continue generating e.h.p.s until their kinetic energies are too low to cause further ionization.

3.2 The Interaction of an X-Ray with GaAs

In general, an X-Ray photon can interact with material in three ways: pair production, Compton and photo-electric interactions[23],[24]. Pair production occurs when a photon disappears, creating an electron-positron pair. In order for this to happen, the photon

must have at least the rest mass energy of the electron and position, 1.02 MeV. A Compton interaction involves a photon scattering from an atom, causing the atom to eject a "Compton" electron and a photon of lower energy. In the photo-electric interaction, a photon is completely absorbed by an atom, and a "photo-electron" is ejected by the atom. In the Compton and photo-electric processes, the atom is left in an excited state.

The X-Rays used to irradiate the GaAs CCD in this study ranged in energy from 8keV to 60keV, much less than the 1.02 MeV needed to create an electron-positron pair. The cross-sections for Compton and photo-electric interactions for incident photons in GaAs with energies ranging from 1 keV to 100 keV are shown in Figure 3.7. The cross-sections were calculated using the "photocoeff" program published by Applied Inventions Corp. Software. The photo-electric interaction is more likely in this energy range, and for photon energies below 30 keV the chance of a Compton interaction is negligible. For the rest of this study, it will be assumed that all photon-solid interactions are photo-electric.

3.3 The Photo-electric Effect

Since a photon is completely absorbed in a photo-electric interaction, the chance, $p(z)$ of the photon being absorbed within a distance dz at a given depth z in a material is given by

$$p(z)dz = \lambda \exp(-\lambda z)dz \tag{3.10}$$

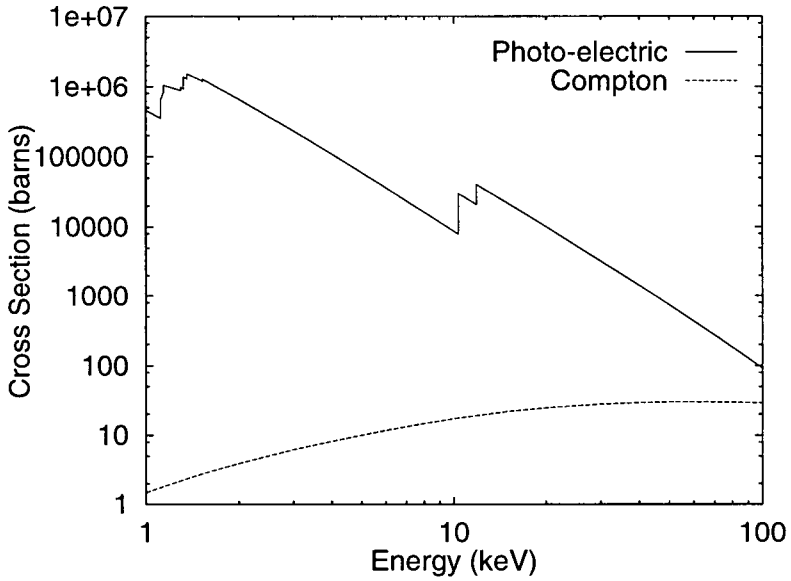

Figure 3.7: The Compton and photo-electric cross section for X-Rays of energies from 1 to 100 keV in GaAs

where λ is the linear absorption coefficient of the X-Ray in the material. Table 3.2 shows the photo-electric linear absorption coefficient for six different X-Ray energies calculated using the "photocoeff" software. The chance, $P(z)$, that a photon has been absorbed by the time it reaches a depth z is given by integrating 3.10 to get

$$P(z) = 1 - \exp(-\lambda z) \tag{3.11}$$

The chance that a K_α photon from the six elements used in this work will be absorbed in 30 μm of GaAs, the depth of the active region in the CCD, is shown in table 3.2

When a photon interacts with an atom by the photo-electric effect, an electron is ejected from one of the inner shells. This ejected electron, the photo-electron, has an energy of $E - E_s$, where E is the energy of the incident photon, and E_s is the binding energy of the shell that the electron has been ejected from. The photon has an ~80%

Table 3.2: Chance for absorption in 30μm of GaAs of a K_α X-Ray from the elements used in this work.

Element	Cu	Rb	Mo	Ag	Ba	Tb
K_α X-Ray energy (keV)[25]	8.047	13.394	17.489	22.162	32.19	44.17
Linear photo-electric absorption coefficient, λ (1/cm)	352.95	649.11	320.32	166.93	58.54	23.02
Chance of absorption	0.653	.857	.617	.394	.161	.067

chance of ejecting an electron from the inner-most, or K, shell and ~19% chance of exciting an electron from the next higher shell, the L shell[26]. The angular distribution of the photoelectrons depends on the velocity, v, of the electron relative to the speed of light, c. If $\beta = v/c$, then the non-relativistic Born approximation gives the partial cross section for an electron to be ejected in a direction given by θ and ϕ as [27]

$$d\sigma(\theta,\phi) \propto \frac{\sin^2(\phi)\cos^2(\theta)}{(1-\beta\cos(\phi))^4} d\theta d\phi \tag{3.12}$$

where θ is the angle between the polarization of the incident photon and the direction of travel of the incident photon, and ϕ is the angle between the direction of travel of the incident photon and the ejected photo-electron. For a non-polarized beam of photons, the angle θ is random, so the angular distribution can be treated as being independent of θ. Figure 3.8 shows the angular distributions in ϕ, with $\theta = 0$, for a photo-electron ejected with small energy ($\beta = 0$) and for a photo-electron with E = 50 keV ($\beta = 0.414$).

The excited atom can relax to its ground state in two ways. The first is for an electron from an outer shell to take the place of the ejected electron, emitting an X-Ray of energy $E_s - E_o$, where E_o is the energy of the outer shell involved in the process. This X-Ray is

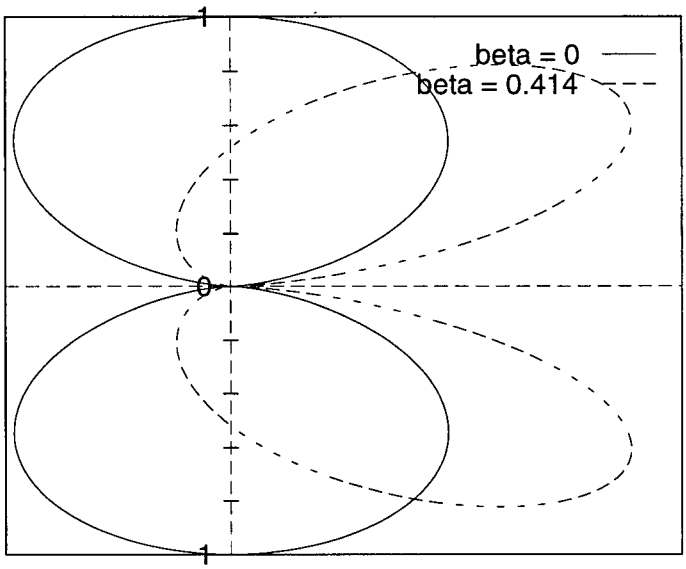

Figure 3.8: The angular distribution in ϕ (with $\theta = 0$) of ejected photoelectrons for $\beta = 0$ and for $\beta = 0.414$, normalized so that the maximum probability is 1.

called a secondary X-Ray. The second method is an Auger process, in which an electron "falls" from an outer shell into the vacancy in the K-shell, ejecting another outer shell electron of energy $E - E_o$ in the process[28]. The ratio of secondary X-Rays to Auger electrons emitted by a given atom is independent of the energy of the incident X-Ray and is called the fluorescent yield. For Ga and As, the fluorescent yields for the K-shell are[29].

Ga - 50.7%

As - 56.2%

3.4 Creation of electron-hole pairs

The photo-electron and the secondary electron created in the photo-electric interaction lose their energy through multiple scattering interactions, creating a large number of electron-hole pairs (see section 3.5). These other electron-hole pairs also scatter and create more e.h.p.s. The process continues until the energy of the ionized electron-hole pairs is a few eV. These low energy electron-hole pairs are unable to cause further ionization, but instead lose energy to lattice vibrations, eventually cooling down to ambient temperature. The average number of electron-hole pairs, N_{ehp}, created in this cascade of electrons by an electron of energy E can be described by the ratio $w = E/N_{ehp}$. The accepted value of w for GaAs is 4.2 eV/e.h.p.[14]. That is, on average it takes 4.2 eV to create a relatively long-lived electron-hole-pair in GaAs.

The creation of electron-hole pairs is a statistical process, so the number of electron hole pairs created by an electron of energy E will not be constant. The variance in N_{ehp} is proportional to N_{ehp}[30]. The constant of proportionality, called the Fano factor, is a function of the material within which the electron interacts. The Fano factor, f, for GaAs as room temperature is quoted as being < 0.18[31].

If none of the energy of an incident photon of energy E escaped from the detector, then the number of electrons seen by the detector would be a Gaussian distribution around a number of electrons $N_{ehp} = wE$. The variance of this distribution would be $\sigma^2 = fN_{ehp}$. The X-Rays used in this study had energies from ~10 keV to ~60 keV,

corresponding to the creation of ~2300 – ~14 000 electron-hole pairs. Using a Fano factor of $f = 0.18$, this gives Gaussian line-widths, 2σ, of ~41 and ~100 e.h.p.s, respectively.

3.5 Interactions of electrons in GaAs

The photo-electrons and Auger electrons created by the incident X-Ray have energies from ~1 keV to ~50 keV. These electrons interact with the electrons and nucleus of the GaAs through many different processes. Elastic interactions occur between the electron and the partially shielded nucleus of the solid's atoms. Slow secondary electrons can be created through interactions with loosely bound conduction electrons in the solid. Faster secondary electrons can also be created through this method, or by interactions with the inner shell electrons of the solid. Another type of interaction, plasmon scattering, occurs when the Coulomb field of the incident electron disturbs the long range correlation in the Coulomb field of the conduction band electrons, exciting collective oscillations of these electrons, called plasmons. All of these interactions are included in the phenomenological "continuous energy loss approximation" of Bethe[32]. This gives the energy loss of an electron per distance traveled, dE/dx, in a material with atomic number Z, density ρ and atomic mass A as

$$\frac{dE}{dx} = 7.84 \times 10^4 \left(\frac{Z\rho}{AE}\right) \log(1.166E/J) \tag{3.13}$$

where E is the energy of the electron and J is defined as the average energy lost in an interaction. An expression for J is given by Berger and Seltzer as[32]

$$J = (9.76Z + 58.5Z^{-1.19})10^{-3} \text{ keV} \tag{3.14}$$

By integrating dx/dE from (3.13) from the initial energy of the electron, E, to 0, one can find the mean distance traveled by an electron of energy E in GaAs. This distance is the mean distance the electron would travel if it did not change its direction of travel through the interactions. The actual displacement of the electron from its starting position will be much less, because of the many scatterings the electron undergoes. Figure 3.9 shows a plot of electron path length, from integrating (3.13), as a function of energy for electrons in Ge. The calculation was done for Ge because its atomic number ($Z = 32$) is in-between that of Ga and As ($Z = 31$ and $Z = 33$), and its density is the same as GaAs.

3.6 Escape of particles from the detector

Not all of the energy of the photon is always absorbed by the detector. This is because the detector has a finite volume, so some of the electrons and photons created in the active region may escape. If we look at the distribution of the number of electrons deposited in a detector for an ensemble of incident photons of equal energy, then the escape of particles will affect the shape of this distribution[34].

This escape of energy can occur through a number of different processes. Either a secondary X-Ray, the photo-electron or an Auger electron can escape from the device.

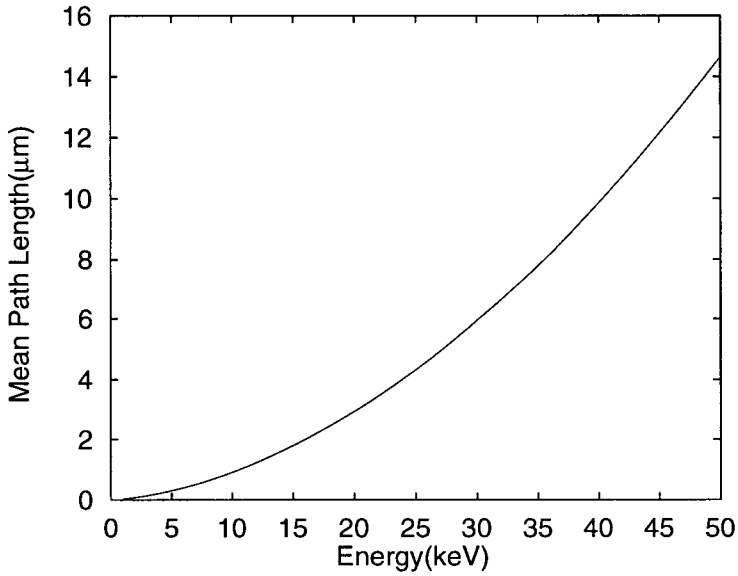

Figure 3.9: The mean path length of an electron in Ge, calculated using the continuous energy loss approximation of Bethe.

When recording the number of electrons, N, collected in a pixel of the CCD due to the absorption of an incident X-Ray of energy E, events where no particles escape will result in a peak at $N = E/w$. When an X-Ray escapes, all of the energy of the X-Ray escapes the detector. The escape of X-Rays of energy E_s will result in a second peak at $N = (E - E_s)/w$. In contrast, the escape of an electron does not always result in the same energy loss; the loss depends on how far the electron has traveled before it leaves the detector. The energy lost ranges from zero (the electron never leaves the detector) to the total energy of the photo or Auger electron (the electron is created right at the edge of the detector and escapes right away). The distribution of the number of electrons deposited in the detector due to electron escape processes will therefore have a tail at lower N. The shape of this tail depends on the geometry of the detector, the angle at

which the photons are incident upon the detector, and the material of which the detector is made (see section 6.5.2 for further discussion).

Chapter 4

Electron Transport

4.1 Introduction

Figure 4.10 shows a time-line of the creation and collection of electron hole pairs in the CCD. The initial interaction between the photon and solid (Figure 4.10-a) and the creation of electron hole pairs (Figure 4.10-b) were discussed in sections 3.2 and 3.5. This chapter will discuss the transport of the e.h.p.s after the initial distribution has been created (Figure 4.10-c and -d). For the purpose of this discussion, two different regimes will be studied: that where all of the e.h.p.s were created in the depletion region, and that where all the e.h.p.s were created in the field-free region.

The high energy photo-electron created by an incident X-Ray will leave a high density track of electron hole pairs in its wake. At first, the electron-hole pairs will spread by ambi-polar diffusion (Figure 4.10-c). What happens next will depend on whether the charge was deposited in the field-free or depletion region. If the charge is in the field-free region, the charge will continue to diffuse until it enters the depletion region, recombines or is trapped. If, however, the charge is in the depletion region, then after ~400 ps the field will fully penetrate the charge distribution and the electrons and holes will start

to drift towards the top and bottom of the CCD, respectively (Figure 4.10-d). It takes ~100 ps for the electrons to drift to the top of the CCD from the bottom of the depleted region. At this point, the electrons become trapped in one of the pixels and they will then be moved towards the output of the CCD, pixel by pixel.

The discussion above makes a simplification: it assumes that the high-energy electron moves in a straight line through the CCD. This, of course, is not what will happen. The electron will be scattered by numerous collisions during its travel. The effects of this scattering on the shape of the distribution were modelled by a Monte Carlo simulation, which is discussed in section 6.5.2. For now, the simplified picture of the electron moving in a straight line is adequate.

4.2 Electrostatic fields in the CCD

The vertical fields in the CCD will be zero except for in the depleted regions near the p^+–p^-, p^-–n and n–Cermet junctions. The field that electrons will drift in is created by the p^-–n junction (see Figure 2.4). With a bias on the substrate of -7 V, the depleted region is 11 μm deep. The field will increase linearly from the zero at the bottom of the depletion region, to a maximum field of $E_{max} = 1.5 \times 10^4$ V/cm at the p^-–n junction and will then decrease rapidly (within 1 μm) to zero field.

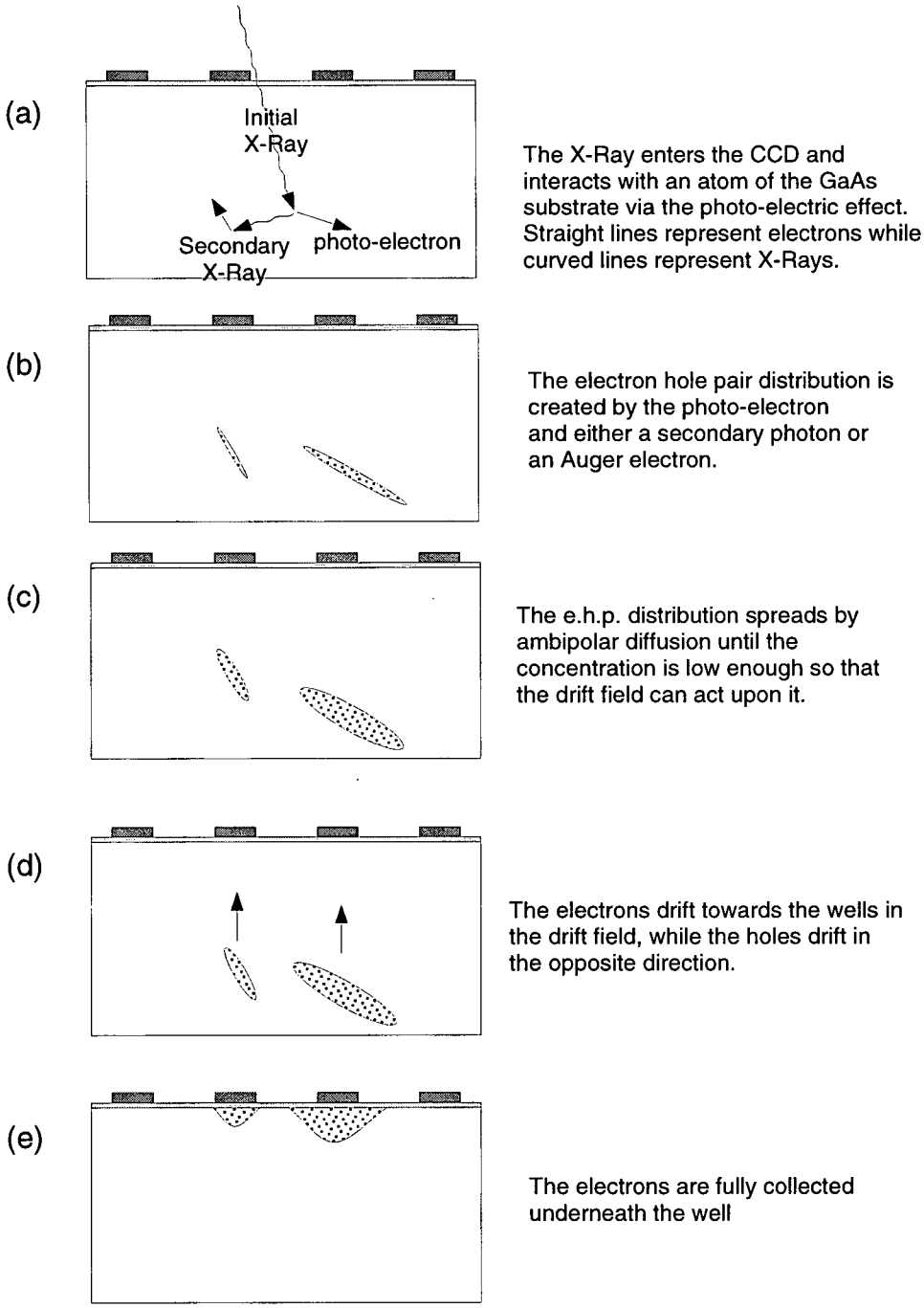

Figure 4.10: A time-line of the creation and collection of electron hole pairs in the CCD

4.3 Initial distribution of e.h.p.s

When the electron-hole pairs created by the incident X-Ray have all cooled down to room temperature, to a good approximation they are distributed in a Gaussian cylinder with a radius of σ = ~0.1 μm along the path of the photo-electron that created them[35]. The density of the electron-hole pairs in the cylinder is approximately Gaussian in the radial direction outward from the axis of the cylinder. The density of e.h.p.s per unit length, N_0, can be found by dividing the energy loss of the electron per unit length, dE/dx, (equation (3.13)) by the average energy needed to create an electron-hole pair in GaAs, w = 4.2 eV. The number of e.h.p.s created in 1 μm by a 30 keV electron in GaAs is 685. The density of e.h.p.s along the axis of the cylinder of charge created by this electron is 1.1×10^{16} cm^{-3} (from equation (4.16)). Figure 4.11 shows a plot of N_0 as a function of x. As the energy of the electron gets lower, the linear density of e.h.p.s increases, until the last 10 keV of energy is deposited in 1 μm. This last micron of charge is so much denser than the rest that a better model of the charge distribution is a ~0.1 μm thick Gaussian cylindrical tail with a length dependent on the initial energy of the photo-electron, followed by a Gaussian ball of charge roughly 0.25 μm in radius. If the photo-electron has an initial energy of less than 10 keV, then there will be no tail.

A simplified picture for the electron motion assumes that the e.h.p.s effectively screen the interior of the distribution from the applied field when the e.h.p. density exceeds the background doping density of the GaAs, ~10^{14} cm^{-3} in our case. Electrons and

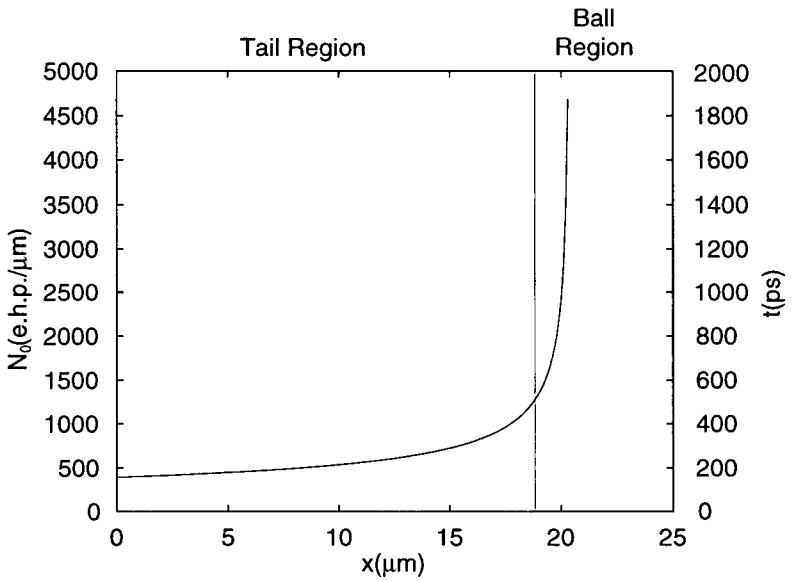

Figure 4.11: The linear e.h.p. density (N_0) and the time (t) required for the initial distribution to diffuse to an on-axis density of 10^{14} cm^{-3} for a 60 keV photo-electron as a function of the distance traveled by the photo-electron.

holes outside of the radius of penetration of the field will be swept towards the top and bottom of the CCD, respectively. Electrons and holes inside of the radius of penetration will undergo ambipolar diffusion. The speed of the diffusion is given by the ambipolar diffusion constant, $D_{\rm ap}$, which is related to the electron and hole diffusion constants, D_n and D_p, in the limit where the electron and hole concentrations are much greater than the donor or acceptor density, by[36]

$$D_{\rm ap} = \frac{2D_nD_p}{D_n + D_p} \tag{4.15}$$

For GaAs, D_n and D_p for an electron or hole density of 10^{16} cm^{-3} are 222 cm^2/s and 10.4 cm^2/s, respectively[21]. This gives an ambipolar diffusion constant of $D_{\rm ap}$ =

19.8 cm^2/s. For the track section of the e.h.p. distribution, the electron-hole pair density, $\rho_{\text{ehp,cyl}}(r,t)$ at a radius r and time t is found by solving the diffusion equation in a cylindrical co-ordinate system to get

$$\rho_{\text{ehp,cyl}}(r,t) = \frac{N_{axis}}{(1+\frac{2D_{ap}t}{\sigma_0^2})} \exp[-r^2/(2\sigma_0^2 + 4D_{ap}t)] \tag{4.16}$$

where N_{axis} is the on-axis density of the e.h.p. track at $t = 0$, and σ_0 is the initial radius of the distribution, 0.1 μm. N_{axis} is related to the linear density of e.h.p.s, N_0, by

$$N_{axis} = \frac{N_0}{2\pi\sigma_0^2} \tag{4.17}$$

The time for the distribution to diffuse will be the largest at the point where the tail of the distribution enters the ball. At this point, the linear e.h.p. density is ~1000 e.h.p./μm. The distribution will diffuse to an on-axis density of 10^{14} cm^{-3} after ~400 ps, and will have a width of ~1.25 μm at this time.

The e.h.p. density in the ball section of the distribution is found by solving the diffusion problem in a spherical co-ordinate system. The solution is

$$\rho_{\text{ehp,ball}}(r,t) = \frac{N_0}{(1+\frac{2D_{ap}t}{\sigma_0^2})^{3/2}} \exp[-r^2/(2\sigma_0^2 + 4D_{ap}t)] \tag{4.18}$$

In this case, N_0 is the concentration of e.h.p.s at $r = 0$ and $t = 0$, and $\sigma_0 = 0.25\mu$m. Solving this equation, it was found that the distribution would take ~320 ps to diffuse to the background density, and the width of the distribution at this time is ~1 μm.

Although a very simplified model has been assumed, we can conclude that the time taken for the applied field to start imparting a drift velocity on the electron cloud is on

the order of a few hundred picoseconds.

4.4 Drift of electrons

Once the electric field has penetrated to the centre of the electron track, all of the electrons drift towards the top of the CCD, while the holes drift towards the substrate. The electrons move at a speed $v_{drift} = \mu_e E$, where μ_e is the mobility of the electrons and E is the electric field acting on them. When the voltage applied to the substrate is -7 V, the depleted region is $x_f = 11$ μm deep, and the maximum field, E_{max}, is 15 kV/cm. This field is larger than the saturation field of GaAs, so μ_e will not be constant. Using the values of v_{drift} as a function of drift field, E, found by Ruth and Kino[37], the drift time across the depleted region,t_{drift}, was found by

$$t_{drift} = \int_{x_0}^{x_f} \frac{dx}{v_{drift}(E(x))} \tag{4.19}$$

t_{drift} was found for the values for the fields and drift depths given in section 4.2. Because the field is zero at $x = 0$, and no diffusion was incorporated in this simple model, the drift time is highly dependent on the value for x_0. For $x_0 = 0.1$ μm, $t_{drift} = 96$ ps. For $x_0 = 1$ μm, $t_{drift} = 74$ ps. These times are of the same order as the time for the initial distribution to diffuse to a point where the field can penetrate the distribution.

The electrons created by an X-Ray will not necessarily all drift into the same pixel. If we ignore the diffusion of the electrons created in the charge column, then each pixel will collect all the charge that is created in a 20 μm region (the length of a pixel) directly

below it. If the line of charge is created below two pixels, then two pixels will have charge drift into them. This is called charge sharing. To make an estimate of the amount of charge sharing in the device due to the length of the initial charge distribution, the scattering of the electron must be taken into account. This is done using a Monte Carlo simulation and discussed in section 6.5.2.

A second kind of charge sharing can occur if a large charge is introduced into the CCD. Too many electrons can affect the potential in the pixels under the CCD, effectively making the wells shallower for additional electrons. If enough charge is added, the electrons will spill over into neighbouring pixels. Additionally, all of the charge in a pixel may not be transferred to an adjacent pixel during the charge transfer process if the charge in the pixel is large. This second kind of charge sharing is much more noticeable with the CCDs used in this study than charge sharing caused by the length of the initial electron distribution (see section 6.9).

4.5 Electrons created in the field-free region

Electrons and holes created in the field free region will not have an electric field to drift in, but instead will only diffuse outward until they either enter the depletion region, recombine or become trapped.

A calculation was made of the time it would take for charge to diffuse from the field-free region to the depletion region. This calculation is, in general, quite complicated, so a number of simplifications were made. First, it was assumed that the field-free region was

infinitely deep. This avoids complications arising from electrons piling up at the field-free – substrate interface. Recombination was ignored, even though it will be a large factor considering the time-scales involved (see section 4.6). Finally, only the ball section of the e.h.p. distribution was considered. Using these assumptions, the time it would take for a percentage of the ball of charge to diffuse to the depletion region was calculated. At most half of the charge will be collected, as the other half will diffuse in the opposite direction. The Gaussian half width, σ, of the ball as a function of time, t, is

$$\sigma = \sqrt{\sigma_0^2 + 2D_{ap}t} \tag{4.20}$$

The fraction of charge, F, from a ball deposited at a initial distance d from the depletion region, which has travelled into the depletion region by time t is given by

$$F = 1/2(1 - \mathrm{Erf}(d/\sigma(t))) \tag{4.21}$$

where Erf(x) is the error function.

Figure 4.12 shows F as a function of time for four different deposition depths, d, of the charge ball. The effects of these e.h.p.s on the spectra seen by the CCD are discussed in section 6.6.

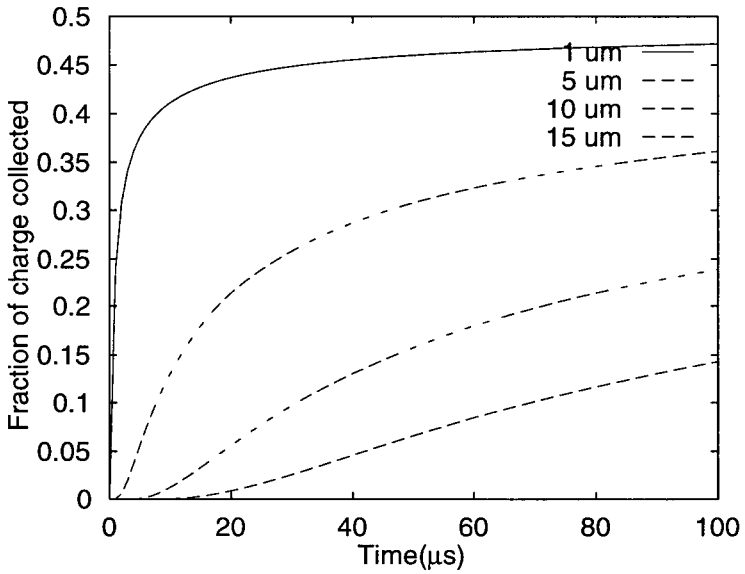

Figure 4.12: The fraction of the total charge of the ball that has diffused into the depletion region as a function of time for $d = 1, 5, 10$ and 15 μm. The curves approach 0.5 asymptotically as at most half of the total charge will diffuse into the depletion region.

4.6 Recombination

According to Nelson and Sobers[38], the radiative recombination lifetime τ_{rad} of an electron in GaAs with an equilibrium electron and hole concentration of n_0 and p_0, respectively, is

$$\tau_{rad} = \frac{1}{B(n_0 + p_0 + \Delta n)} \tag{4.22}$$

where Δn is the concentration of excess electron hole pairs and B is the radiative recombination coefficient. Nelson and Sobers found B to be 3.7×10^{-10} cm^3/s. There are two different densities at which recombination could in principle be important. The first corresponds to the initial diffusion of the distribution from its initial density of Δn ~10^{16} cm^{-3} to the background density, and the second corresponds to the diffusion of

e.h.p.s in the field-free region with Δn~10^{14} cm^{-3}. For an excess electron population of 10^{16} cm^{-3} in GaAs doped at $N_A = 10^{14}$ cm^{-3}, $\tau_{rad} = 250$ ns. This time is large compared to the time for the electron-hole pairs to diffuse from their initial distribution to the background hole concentration, so recombination should not be a factor during the ambipolar diffusion of the initial distribution of the e.h.p.s or the drift of the e.h.ps in the depletion region. The radiative recombination lifetime for e.h.p.s at a concentration of $\Delta n = 10^{14}$ cm^{-3} in the field free region is ~14 μs. As discussed in section 4.5, this is small compared to the diffusion time for the e.h.p.s created at depths greated than 11 μm in the device (see figure 4.12). Recombination will therefore be a large factor for e.h.p.s created in the field-free region.

4.7 Summary of transport processes

The important length scale in the CCD is the pixel pitch of 20 μm. If the ball of charge is deposited in the drift region, then it will have a width of $\sigma \simeq 1.5$ μm, which is not significant compared to the pixel width. If however, the ball is deposited in the field-free region, then it will have a width of up to a few pixel lengths by the time an appreciable fraction of the charge in the ball enters the depletion region.

There are three important time-scales in the CCD. The first is the clock period of 0.1 μs. The second is the frequency of X-Ray events in the CCD of ~1 Hz. The third is the radiative recombination lifetime of electron-hole pairs, ranging from 250 ns at an e.h.p. concentration of 10^{16} cm^{-3} to 14 μs at an e.h.p. concentration of 10^{14} cm^{-3}. If the e.h.p.s

are deposited in the depletion region, they will be quickly swept into the well of the CCD and then transported to the output. This will all occur within ~500 ps, much smaller than all of the relevant time-scales. If, on the other hand, the e.h.p.s are deposited in the field-free region, there will be a period of diffusion before any of the electrons encounter the drift field. These diffusion times of ~100 μs are long compared to both the clock period and the recombination lifetimes, but are still smaller than the X-Ray event frequency. Because the diffusion times are large compared to the recombination times, the charge that will make it to the wells of the CCD will be greatly reduced. Because the diffusion times are large compared to the CCD clock's period, the charge that does make it to the well will be spread over hundreds of pixels. These two factors make it unlikely that any charge that is deposited at any depth larger than a micron in the field-free region will contribute to the spectra in the CCD.

Chapter 5

Experiment

5.1 Experimental Setup

The CCD is run at room temperature at a frequency of 10 MHz, with a substrate voltage of −7 V. This substrate voltage was chosen as it was the largest that was believed to be usable without harming the CCD. The output of the CCD with no input signal consisted of a square wave centred around zero volts with a peak to peak voltage of 620 mV. The frequency of the pulses was the same as the input clock, 10 MHz. The area of each pulse above a threshold represented a signal proportional to the charge transferred out of the last pixel of the CCD.

The output of the CCD was sent to a Tektronix DSA 602 digital sampling oscilloscope. Data was acquired using a Personal Computer that was connected to the oscilloscope by means of an IEEE 488 interface. The computer set the trigger level on the oscilloscope using an algorithm described below, waited for a number of traces to be read into the oscilloscope's memory, and then down-loaded the traces off of the oscilloscope. The trigger level on the oscilloscope was then reset, and the whole process repeated.

The oscilloscope's voltage settings were set to 5 mV/division, and the time scale was

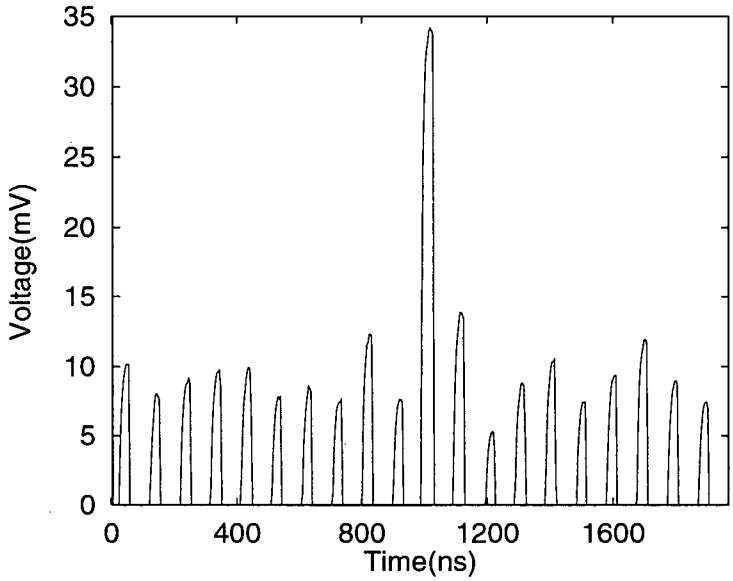

Figure 5.13: A typical oscilloscope trace for an event triggered by a 44 keV X-Ray from a Tb foil. There are 20 peaks shown in the trace, and the signal peak is the 11th peak shown. Peaks 1 and 22 from the original trace were trimmed off by the analysis software.

set to 50 nS/div. The voltage was offset so that only the bottom of the CCD waveform was viewed. This is because the peak-to-peak voltage of the waveform was 620 mV, and a typical signal ranged from 5 mV to 45 mV for the 10–60 keV X-Rays used in this study. All of the analysis was done with a more negative voltage denoting a larger signal on the CCD. The trigger point was set so that exactly 22 pulses showed on each trace. Figure 5.13 shows a typical oscilloscope trace triggered by a 44 keV K_α X-Ray from Tb.

The trigger level of the oscilloscope had to be carefully set for a number of related reasons. First, the event rate (~1 Hz) was much smaller than the clock rate of the CCD (10 MHz). Secondly, the peak to peak voltage of the CCD output drifted appreciably during the two to six hours needed to sample 20,000 events. Thirdly, the size of the

signals on the CCD (5 – 45 mV) was much smaller than the peak to peak voltage of the CCD's output waveform (620 mV). Putting all these factors together meant that the trigger level had to be above the level of the CCD's output when there were no events, but not so high as to discriminate against low energy events. The trigger level also had to be high enough to avoid falling into the noise if the CCD's output drifted higher, and was therefore reset periodically to take into account the drift.

The trigger level was determined by first setting it low enough that the oscilloscope would be triggered on every pulse from the CCD. An envelope of 512 scope traces was taken. This envelope showed the range of the voltages for each point on the oscilloscope over the 512 traces that were taken. Because the rate of the CCD was much larger than the rate of events from the sources, this gave an envelope of the pulses from the CCD without any events. The maximum height of each peak on the trace was found, and these maxima were averaged. By using this average, a measure of the top of the CCD waveform was found. An offset, either positive or negative, was then added onto this average. The offset was chosen so that the maximum trigger rate was achieved without triggering off of non-event peaks (see section 6.2). The offset also had to be large enough that any drift of the CCD's output levels would not cause the oscilloscope to trigger off of every pulse from the CCD. The trigger level of the oscilloscope was then set to the result.

After the trigger level was set, the oscilloscope was instructed to take 900 readings (the maximum number of traces that it could hold in memory at the resolution used was

912). After the readings were done, the traces were loaded into the computer, the trigger level was reset using the same procedure as above, and the process was repeated.

The resetting of the trigger level was done to reduce the effects of drift in the absolute CCD voltage level. The time between settings of the trigger varied from 2 minutes to 25 minutes depending on the event rate, and hence on the X-Ray source used to irradiate the CCD.

5.2 Analysis of oscilloscope traces

Each individual oscilloscope trace was analyzed to find the charge deposited in the CCD, as represented by that trace. The first and last peak were discarded, leaving twenty pulses to analyze. The charge of each peak was found by integrating the voltage over the whole peak. Each peak was denoted as either being part of the signal or part of the background. The time-base on the oscilloscope was set so that peak 12 was the peak that triggered the oscilloscope. Because of this, Peak 12 was defined as the central signal peak, and a number of peaks on either side of it could also be considered as signal peaks. If the number of signal peaks, N_{signal}, was chosen to be 5, then peaks 10–14 were considered signal peaks. The peaks that were not signal peaks were considered background peaks. The background level was found by finding the average charge of the background peaks. The net signal contained in a trace was found by summing the charge of the signal peaks, and then subtracting the background.

Problems in the above algorithm occurred when any of the peaks in the trace went off

the screen of the oscilloscope. A 7-bit number was used to store the position of each point on an oscilloscope trace, with the top of the screen set to read 127 and the bottom of the screen 0. When the peak went off the top of the screen, the 8-bit number "rolled-over", becoming a large negative number. This caused the peak finding routine to find spurious peaks, which, in turn, caused the traces in the rest of the file to be read improperly. To avoid this problem, any traces that had peaks within 5 units of the top of the screen were discarded, with 128 units being the full extent of the screen.

The final step in the analysis was to create a histogram of the charges deposited in the CCD. The bin size of the histogram was set to five charge units (C.U.), with the scale of the histogram going from 0 C.U. to 2000 C.U. The charge unit scale is essentially arbitrary, and should only be used to compare different spectrum on the same CCD, obtained using the same system parameters.

5.2.1 The Choice of N_{signal}

The choice of N_{signal} can have a large effect on the shape of the spectrum found by the CCD. Figure 5.14 shows the the spectrum from the characteristic X-Rays of Tb analyzed from the same raw data using $N_{signal} = 3, 5, 7$ and 9. The reduced data was fit to three peaks, labelled peak 1, peak 2 and peak 3, whose parameters are shown in table 5.3. If the charge in a single event were contained in one pixel of the CCD's output, changing N_{signal} would have little effect on the shape of the spectra. In fact, if the number of pixels that contain charge from an event is $N_{charged}$, then for $N_{signal} > N_{charged}$, there should be

Table 5.3: The area (A), width (w) and position (x) of the first and third peaks for Tb data analyzed with N_{signal} = 3, 5, 7 and 9. The areas are expressed in units of 1000 Charge Units counts. The ratio between the area of the first and third peaks and the resolution of the third peak are also shown

N_{signal}	First Peak			Third Peak			ratio	Resolution
	A	x (C.U.)	w (C.U.)	A	x (C.U.)	w (C.U.)	(%)	(keV)
3	21	662	269	37	1051	214	57	12.4
5	40	790	481	129	1090	226	31	13.0
7	9.6	744	281	47	1156	239	20	13.8
9	9.8	810	305	48	1206	257	20	14.8

no change in the signal charge calculated by the analysis program. The change in the shape of the spectra from N_{signal} = 3 to N_{signal} = 5 is quite large, and the change for N_{signal} larger than 5 is much smaller. This suggests that the charge in a signal from a Tb X-Ray is contained in at most five pixels, and that some events have more than three pixels with charge in them. The data was analyzed with N_{signal} = 5, a choice that was a trade-off between the decrease in resolution as N_{signal} was increased and the increase of the area of peak 1 as N_{signal} was decreased.

5.3 Tests with known input pulses

This experiment studied the relationship between the charge deposited in the CCD and the number of charge units found by the analysis of the oscilloscope traces. A known input pulse was applied to the first gate finger of the CCD, in order to introduce a charge into the active layer under the first pixel. The charge pulses were 4 ns wide, and ranged

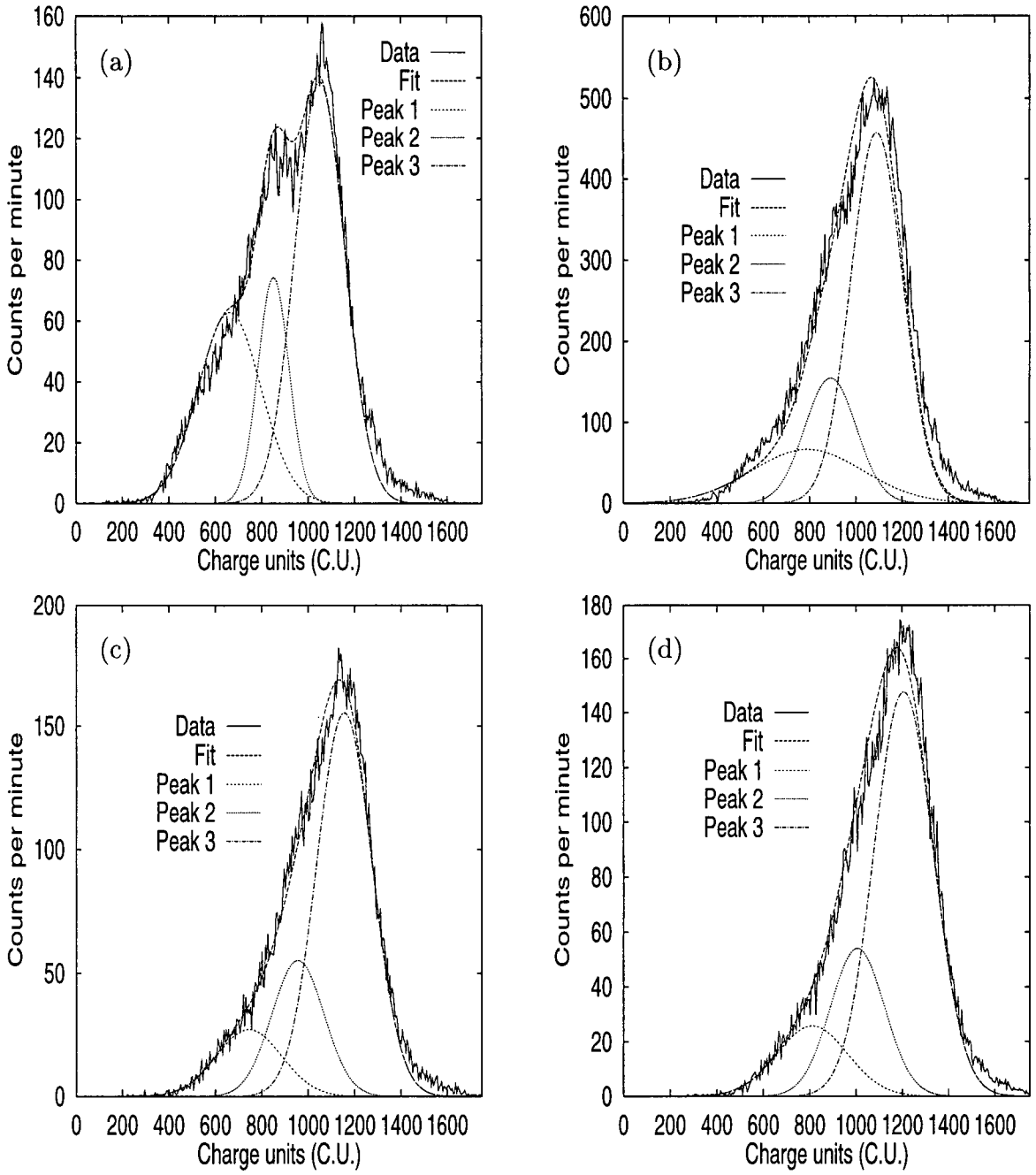

Figure 5.14: The spectra of Tb X-Rays analyzed with N_{signal} = 3, 5, 7 and 9 shown in figures (a), (b), (c) and (d) respectively.

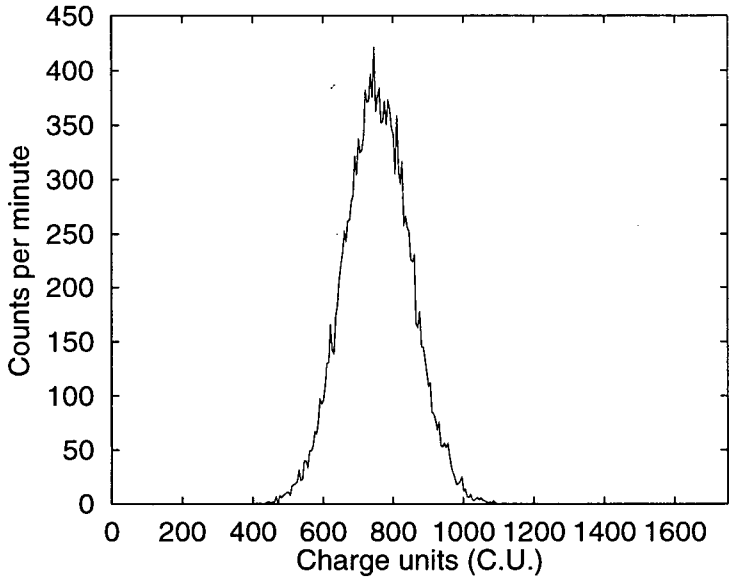

Figure 5.15: A histogram of the count rate for a 31mV input pulse

from 0 mV to 44 mV in height. The signals were then analyzed as described above, and histograms for each input voltage were made. A histogram for an input voltage of 31 mV is shown in Figure 5.15.

The histograms were then fitted to Gaussians with an area A, position x_0 and width, $w = 2\sigma$, where σ is the half-width of the Gaussian. A plot of the charge units deposited in the CCD as a function of the input voltage is shown in figure 5.16. A 2^{nd} order, concave up polynomial fit was made to the data. It is not known whether or not this non-linearity arises from the input or the output, but the linearity of the charge deposited in the CCD as a function of X-Ray energy (see section 6.3.1) points to the input as the source of the non-linearities.

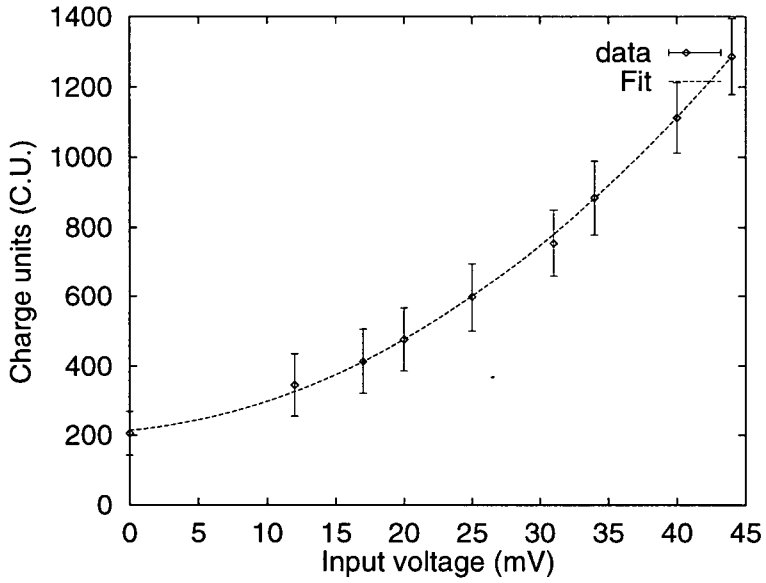

Figure 5.16: The charge deposited in CCD2 by a known input pulse as a function of the height of the pulses, analyzed with $N_{signal} = 5$. The error bars are the Gaussian widths of the peaks. The fitting equation of Q in Charge Units as a function of the input voltage V is Q = 214 C.U. + 3.7 V + 0.47 V^2

The resolution of the detector at each input voltage is found by

$$R = \frac{\Delta E}{E} \tag{5.23}$$

where ΔE is the width, 2σ, of the Gaussian fit to the peaks on the histogram, and E is the position of the maximum of the Gaussian, x_0, on the histogram. A plot of the resolution of the CCD as a function of the position of the peak is shown in figure 5.17 for the known input pulses. A linear fit was made to the plot of $\log(R)$ as a function of the Log of the peak position, $\log(P)$. Raising each side to the power of 10 gives the power relation between R and P (with P expressed in C.U.) of

$$R = 96P^{-0.89} \tag{5.24}$$

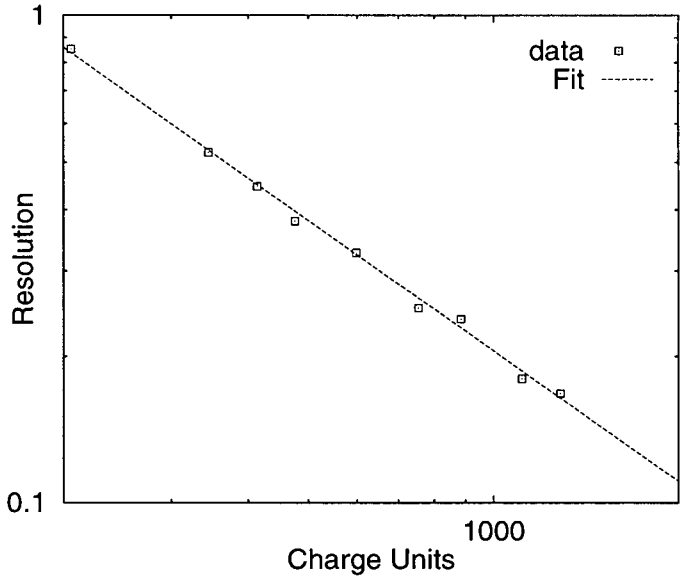

Figure 5.17: The resolution of the charge deposited in CCD2 by a known input pulse as a function of the height of the pulses. The data was analyzed with $N_{signal} = 5$.

Assuming the charge injected into the CCD is constant for a given input voltage, equation (5.24) gives the maximum resolution of the CCD under the operating conditions.

5.4 Response of the detector to Characteristic X-Rays

The response of the detector to the characteristic X-Rays from six elements was studied. A schematic diagram of the source used to create these X-Rays is shown in figure 5.18. The X-Rays from an ^{241}Am source were shone on a foil of one of six different elements. The element then emitted its characteristic X-Rays. The six elements used were (in order of increasing K_α X-Ray energy) Cu, Rb, Mo, Ag, Ba and Tb. The energies of the K_α X-Rays of these elements range from 8.047 keV for Cu to 44.47 keV for Tb. Table 5.4 shows a listing of the K_α energies for all six elements[25]. The source was shone on the

Table 5.4: The K_α energies of the elements used in this study

Element	Cu	Rb	Mo	Ag	Ba	Tb
K_α X-Ray Energy (keV)[25]	8.047	13.394	17.489	22.162	32.19	44.17

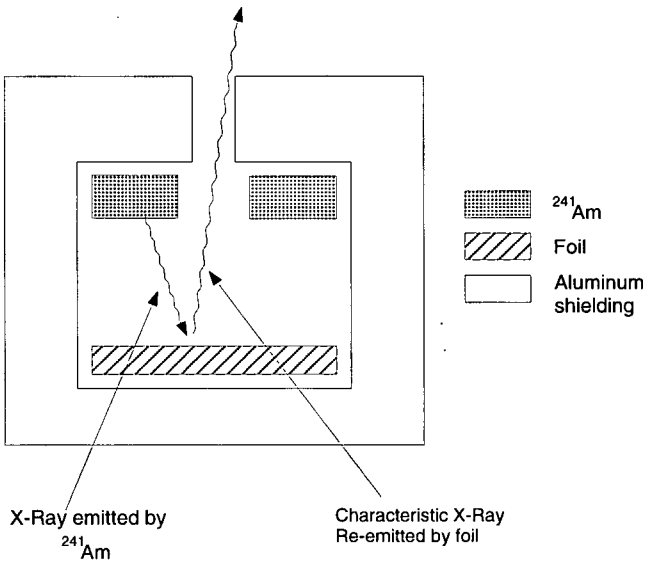

Figure 5.18: A schematic of the source used to create characteristic X-Rays. The ^{241}Am is an annulus. X-Rays emitted by the ^{241}Am are absorbed by the foil, and the foil emits a characteristic X-Ray. Any X-Rays emitted by the ^{241}Am that do not strike the foil will be absorbed by the Aluminum shielding.

CCD from the top. The CCD was covered with a ceramic lid, which had a hole milled in it to allow the X-Rays to impinge on the CCD. The hole was covered with electrical tape to prevent ambient light from shining on the CCD. Figure 5.19 shows a schematic of the setup used to study characteristic X-Rays.

Tests with the single X-Ray energy source were done with two different CCDs that will be referred to as CCD1 and CCD2. A run of 20,000 events was taken with each of the X-Ray energies. Figure 5.20 shows the spectrum for Mo K_α X-Rays on CCD1 and

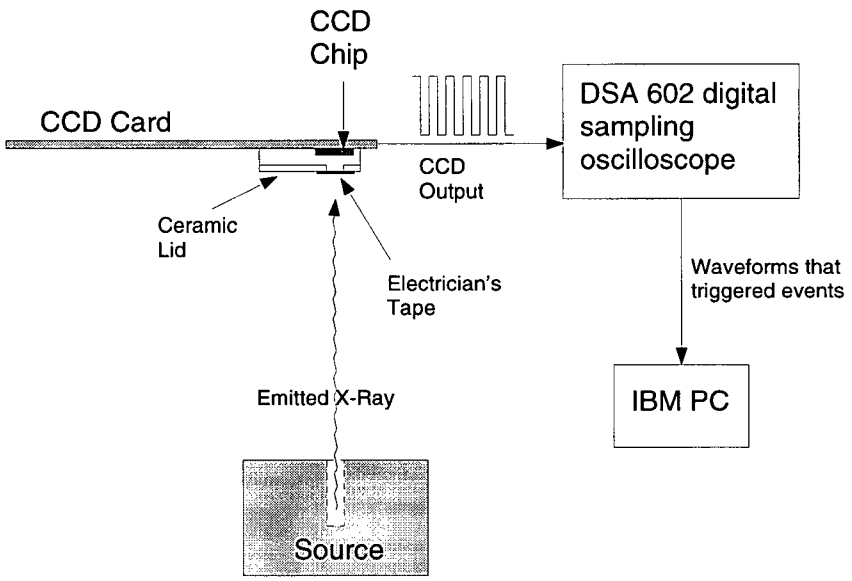

Figure 5.19: A schematic of the experimental setup used to study the X-Ray spectra.

CCD2. Figure 5.21 shows the spectrum for Tb K_α X-Rays on CCD2. All the histograms were made with $N_{signal} = 5$.

5.5 The ^{241}Am spectrum

The response of the detector to the X-Rays emitted by an ^{241}Am source was also studied. The X-Rays were shone on the top of the CCD, and a run of 72 000 counts was taken. Figure 5.22 shows the histogram of the ^{241}Am spectrum found using CCD2 analyzed with $N_{signal} = 5$ and 7. The two values of N_{signal} were used to make sure that the increased energies in the ^{241}Am spectrum did not create charge sharing among more than five pixels, thereby increasing the value needed for N_{signal}. The change in the relative intensities of the peaks was not large, so N_{signal} did not need to be increased.

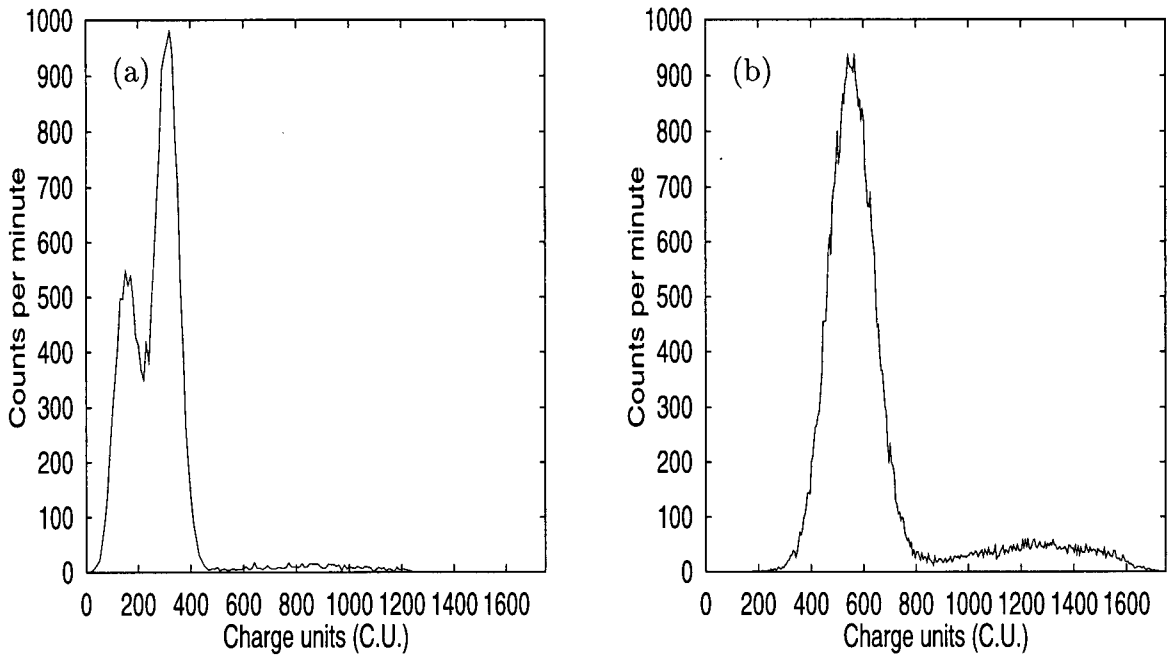

Figure 5.20: The charge deposited in (a)CCD1 and (b)CCD2 by the characteristic X-Rays of Mo, analyzed with $N_{signal} = 5$.

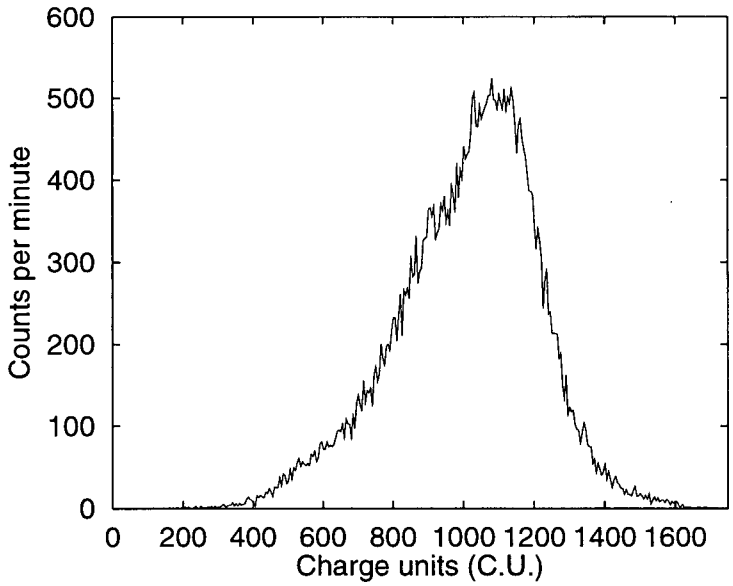

Figure 5.21: The charge deposited in CCD2 by the characteristic X-Rays of Tb, analyzed with $N_{signal} = 5$.

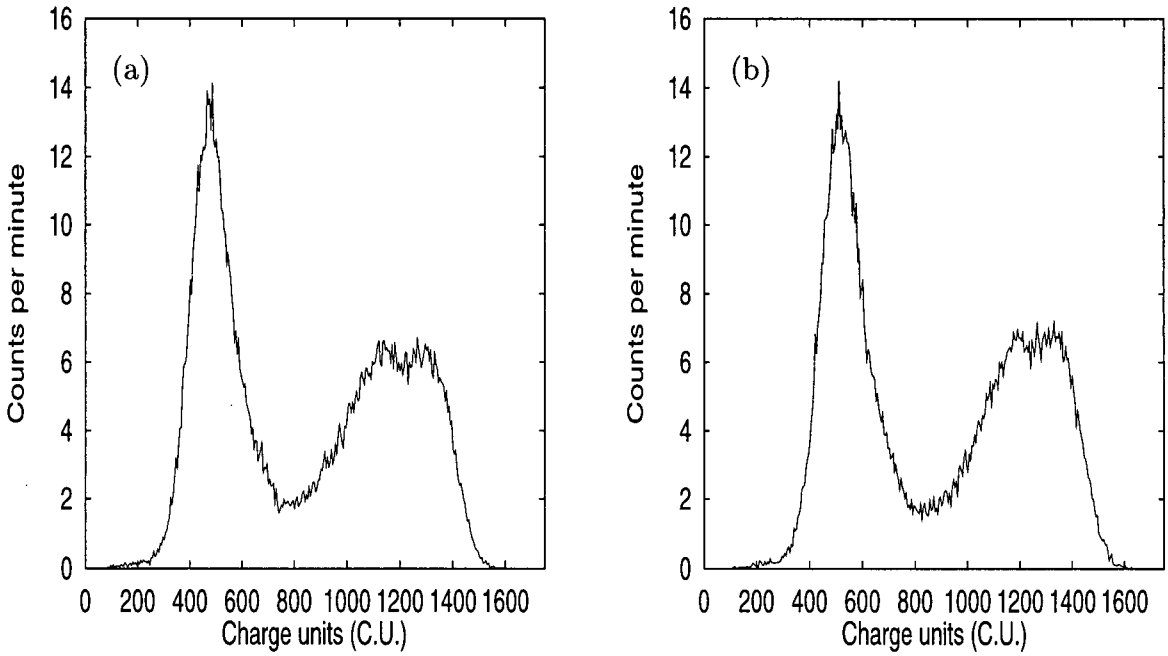

Figure 5.22: The charge deposited in CCD1 by X-Rays from an ^{241}Am source, analyzed with N_{signal} = (a)5 and (b)7.

Chapter 6

Results and Discussion

6.1 Overview

The histograms resulting from the known input pulse studies resulted in single peaks with Gaussian profiles. The histograms for the characteristic X-Rays were not as simple. The histograms for CCD1 all showed at least two peaks. The peak at the low end of the scale stayed at the same position for all the X-Ray energies. This peak, denoted the noise peak, was assumed to arise from events that were caused by triggers due to random noise in the CCD's waveform, rather than triggers from actual events in the CCD. The histograms for Rb, Mo and Ag showed a second peak that, as will be shown in this chapter, varied linearly in position as the energy of the incident X-Ray was changed. This peak was therefore denoted the signal peak. A broad peak at high energies was also evident. It was not considered to be an artifact of the triggering, but instead a result of some higher energy X-Rays being released by the source (see section 6.4). It was called the high energy peak. For the Ba and Tb runs on CCD1, the picture was still more complicated. The noise peak was still evident, but in these cases there were two peaks whose position varied linearly with energy. In section 6.5.1 we present evidence that the

second, lower energy signal peak arises from the escape of secondary X-Rays from the CCD (see section 6.5.2). This second, lower energy peak was therefore denoted the escape peak. The histogram for the Tb X-Ray showed yet another peak, tentatively identified as the field-free peak (see section 4.5) resulting from The escape of photo-electrons from the depletion region of the CCD.

6.2 The Noise Peak

All of the histograms for CCD1 showed at least two peaks. The peak at the low end of the scale stayed at the same position for all the X-Ray energies. This peak was assumed to arise from events that were caused by triggers due to random noise in the CCD's waveform, rather than triggers from actual events in the CCD. Figure 6.23 shows the spectrum of Ag for CCD1 and CCD2. The runs with CCD2 show no evidence of the noise peak. This is because the noise levels in the CCD waveform in CCD2 were larger, causing the trigger level to be raised much higher in the CCD2 runs than the CCD1 runs. This change in the trigger level could have been large enough to avoid any triggers in the CCD waveform, causing the loss of the noise peak in the spectra. A second set of runs for CCD2 was also run with the trigger level set lower. A small noise peak is evident in the Rb and Ba runs, showing that the noise peak is present on CCD2, with its strength depending on the setting of the trigger level. Table 6.5 shows the peak positions and widths for the noise peaks of the K_α spectra obtained with CCD1.

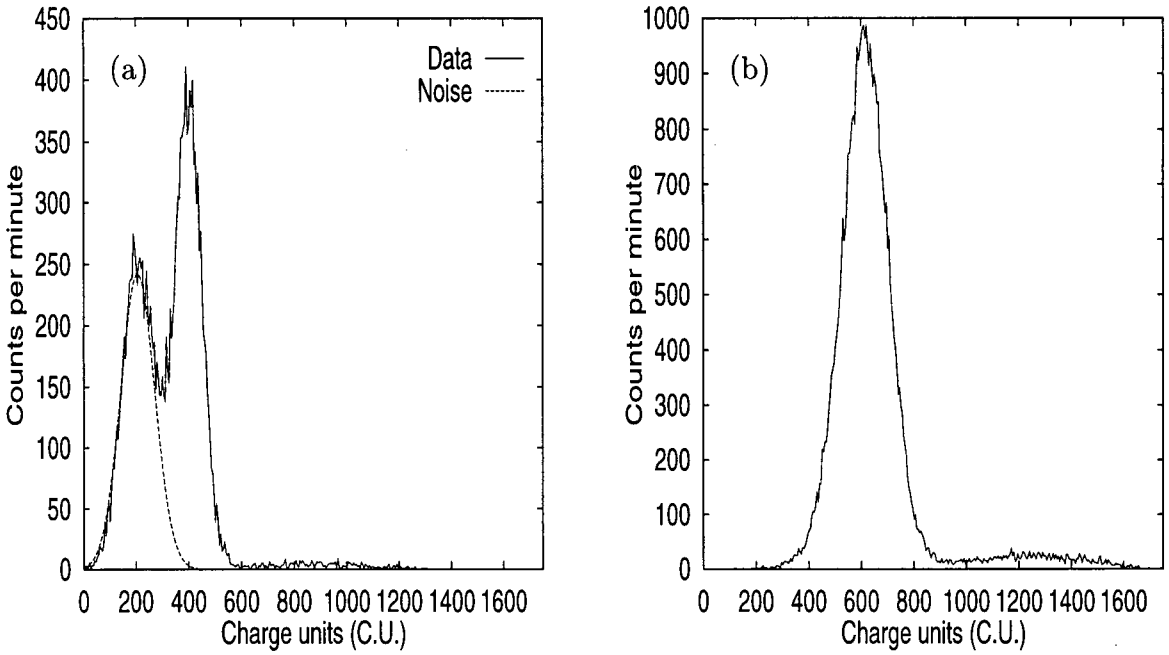

Figure 6.23: The spectra for the K_α X-Rays from Ag on (a)CCD1 and (b)CCD2. The spectrum for CCD1 shows the noise peak, while that for CCD2 doesn't.

Table 6.5: The peak positions (x), areas (A) and widths (w) of the noise peaks in the spectra arising from characteristic X-Rays impinging on CCD1 analyzed with N_{signal} = 5. The areas are in units of 1000 Charge Unit Counts, while x and w are expressed in Charge Units.

Element	A	x	w
Rb	51	172	111
Mo	68	161	99
Ag	40	207	131
Ba	25	200	142
Tb	26	160	89

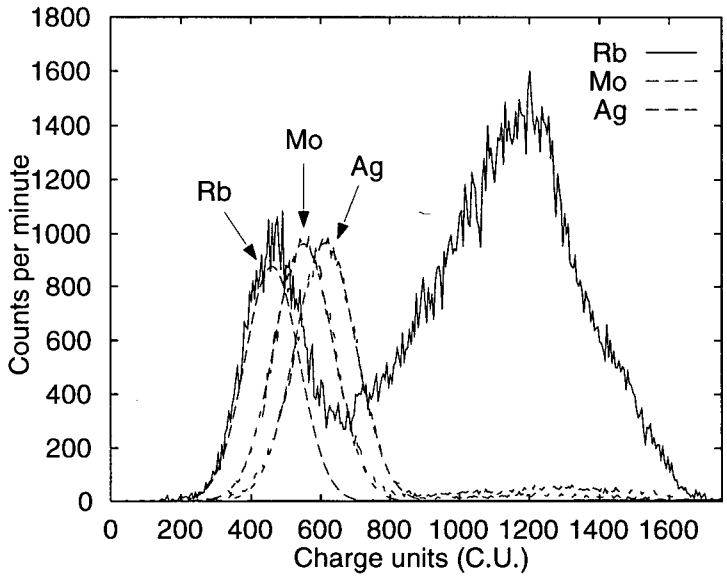

Figure 6.24: The signal peaks, indicated by arrows, for the K_α X-Rays of Rb, Mo and Ag on CCD2. The spectra have been scaled vertically to make comparison easier. The higher energy feature, which is present in all the spectra but most prominent for the Rb spectrum, is discussed in section 6.4.

6.3 The Signal Peak

The signal peak was, as expected, evident in all the spectra. Figure 6.24 shows the signal peaks for the K_α X-Rays of Rb, Mo and Ag incident on CCD2. The positions of the signal peaks, as is shown below, vary linearly with the energy of the incident X-Ray.

6.3.1 Calibration of the CCD Energy Scale

The positions of the signal peaks for the known energy X-Rays were used to calibrate the energy scale of the CCD. Plots of signal peak position in charge units as a function of incident X-Ray energy were made for the runs on CCD1 and CCD2 with $N_{signal} = 5$. The plots are shown in figure 6.25, and the positions are tabulated in Table 6.6. The plots

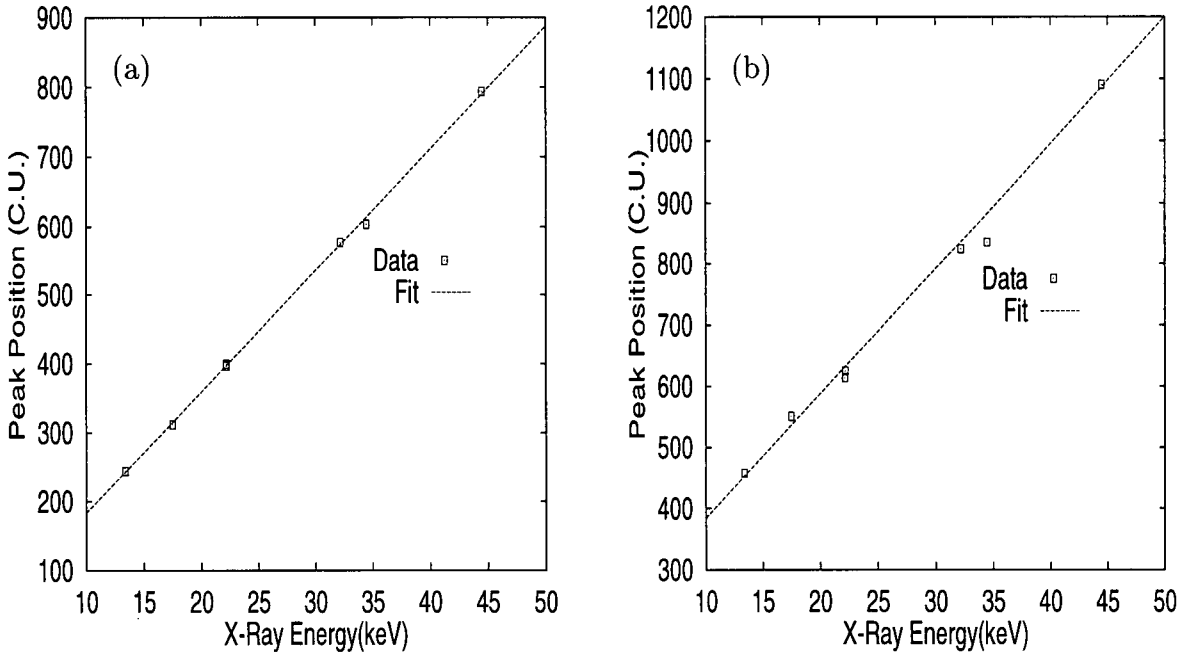

Figure 6.25: Signal peak positions of the known energy X-Rays for (a)CCD1 and (b)CCD2 from the data analyzed with $N_{signal} = 5$. For CCD1, the fitting function of the peak position, P as a function of the energy E of the incident X-Ray is $P = -6.1$C.U.$+19$C.U./keV E. For CCD2, the fitting function is $P = 197$ C.U.$+20$ C.U./keV E.

are linear, showing that the output of the CCD is linearly proportional to the charge in a pixel and that the charge collection efficiency is constant over this energy region.

The resolutions for the signal peaks of the K_α rays from the five elements studied, analyzed using three and five peaks as the signal peaks, are also shown in table 6.6. The resolution decreases as the energy increases, but the width of the peaks is not constant. The resolution is also better for $N_{signal} = 3$ than 5, but setting $N_{signal} = 3$ creates artefacts at higher energies.

Table 6.6: The resolution and position of the signal peaks of the five different incident X-Ray energies from the runs on CCD2, analyzed using $N_{signal} = 3$ and 5.

Element	Rb	Mo	Ag	Ba	Tb	^{241}Am
K_α X-Ray energy (keV)	13.4	17.5	22.2	32.2	44.2	60
N_{signal}=3 position (C.U.)	424	493	556	783	1083	–
N_{signal}=3 resolution	36.7%	36%	36%	24%	14%	–
N_{signal}=5 position (C.U.)	461	554	615	845	1092	1325
N_{signal}=5 resolution	57%	46%	42%	28%	28%	13.6%

6.4 The High-Energy Peak

The Ag spectrum in figure 6.24 also exhibits a broad feature at higher energies (between ~900 – 1600 C.U.). All of the low energy K_α X-Ray spectra (Cu, Rb, Mo and Ag) contained this feature, denoted the high-energy peak (HEP). It is believed that this HEP peak is likely also present in the higher energy K_α spectra, but at higher energies the larger intensity of the signal peak masks it.

Figure 6.26 shows a comparison of the high energy peak in the Cu and Rb spectra taken using CCD2. The Rb spectrum shows both a signal and high-energy peak, while Cu shows only the high-energy peak. The Cu K_α X-Rays were not only low in intensity, but their energy was of the same order as the noise in the CCD, so they were discriminated against, leaving only the high-energy events. The HEPs for Cu and Rb match almost perfectly. The HEPs of Mo and Ag do not match as well, but there are relatively fewer counts in this region of the spectrum for these energies, as the signal peak was much more intense.

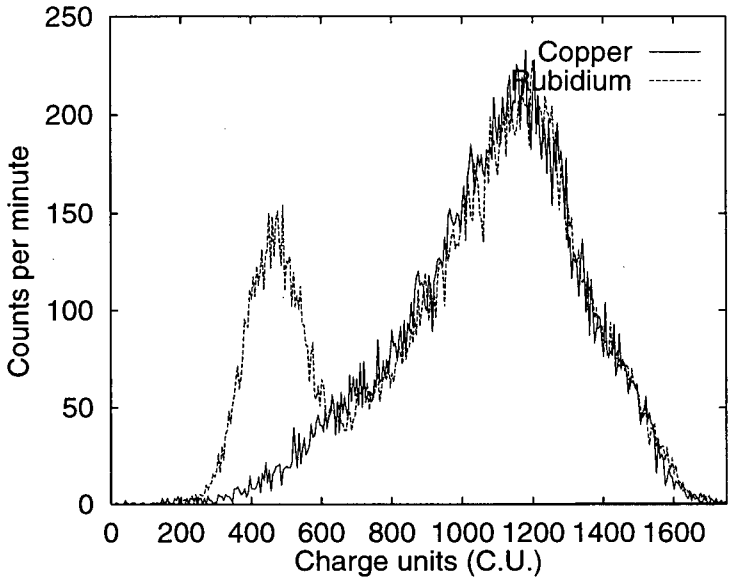

Figure 6.26: Comparison of the high energy region for the Cu and Rb Spectra for runs on CCD2 analyzed with $N_{signal} = 5$. The y-axis was rescaled for the Rb data to allow a direct comparison of the shape of the spectra.

Table 6.7 shows the areas, positions and widths of the HEPs for X-Ray spectra on CCD2. Using the calibration made in section 6.3.1 for CCD2, the high-energy peak was found to be at 50 keV, which is more energetic than any of the K_α X-Rays studied, but lower than the calibrated energy of the 60 keV ^{241}Am X-Ray (see section 6.8.2). The high energy peak could result from back-scattered 60 keV ^{241}Am X-Rays. At 60 keV, both the Compton and coherent scattering cross-sections are ~7% of the photo-electric cross-section.

Table 6.7: The peak positions (x), areas (A) and widths (w) of the high-energy peaks in the spectra arising from characteristic X-Rays impinging on CCD2 analyzed with $N_{signal} = 5$. The areas are in units of 1000 Charge Unit Counts, while x and w are expressed in Charge Units.

Element	A	x	w
Cu	98	1160	387
Rb	156	1169	388
Rb (run 2)	76	1071	509
Mo	33	1226	541
Ag	14	1227	450
Ba	35	1189	381
Ba (run 2)	32	1195	335

6.5 The Escape Peak

Both the Ba and Tb spectra from CCD1 and CCD2 showed a similiar low-energy shoulder whose position varied linearly with the energy of the X-Ray. Figure 6.27 shows the Ba and Tb spectra on CCD2 fit with signal peaks. The position of the signal peak as well as the peak that creates the shoulder are indicated. The differences between the signal and shoulder position are the same for both spectra. It was postulated that this shoulder arose from the escape of photo-electrons and secondary X-Rays from the CCD. To help assign this feature, the escape of secondary X-Rays and photo-electrons was modeled. The escape of secondary X-Rays was studied by finding the chance of escape of an X-Ray interacting at any position in the active area of the CCD. To study the escape of photo-electrons, a Monte-Carlo simulation of the scattering of the photo-electron in the detector was made. This simulation allowed one to determine the spectrum of energies

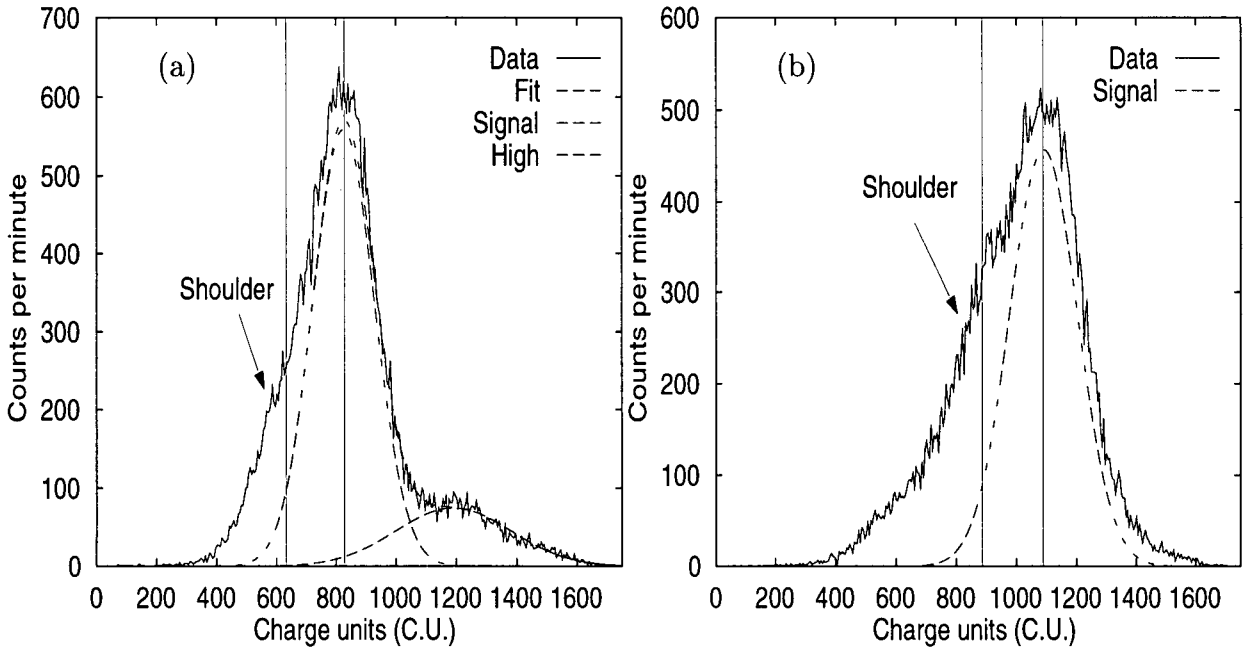

Figure 6.27: The spectrum for (a)Ba and (b)Tb K_α X-Rays on CCD2 analyzed with $N_{signal} = 5$, fitted with the signal peaks. The positions of the signal and the gaussian creating the shoulder have been labeled with vertical lines. The shoulder has also been indicated with an arrow.

deposited in the detector by electrons that escaped from the detector.

6.5.1 Escape of Secondary X-Rays

The active area of the CCD is a 30 μm x 50 μm x 2.5 mm block of GaAs. If a photon of energy E is a distance R from the edge of the active region, then its chance of escape, $P(R)$, is given by

$$P(\lambda, R) = \exp(-\lambda R) \tag{6.25}$$

where λ is the linear absorption coefficient of a photon of energy E in GaAs. The distance R is dependent on the initial position of the photon, $\vec{X}$, and its direction of travel, defined

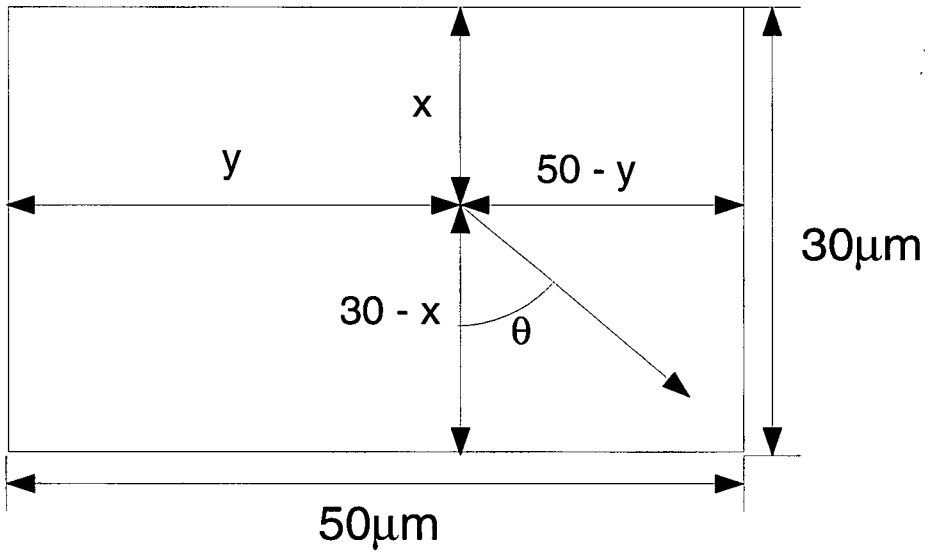

Figure 6.28: A cross section of the CCD, showing x, y and θ. The z-axis is out of the page, and ϕ is the angle from the z-axis.

by two angles, θ and ϕ. We can write R as

$$R = R(\vec{X}, \theta, \phi) \tag{6.26}$$

Figure 6.28 shows a cross-section of the CCD. The figure shows how θ and ϕ are defined, and also shows the components of $\vec{X}$, x and y. The third component of $\vec{X}$ is ignored as it is along the 2.5 mm long axis of the CCD, and is effectively infinite for the photon energies considered here. We can now write R as $R(x, y, \theta, \phi)$.

The photon must escape from one of the four sides of the rectangle (top, bottom, left or right). The chance that a photon will escape from an initial position $\vec{X}$, $P(\vec{X})$, is found by integrating over all angles θ and ϕ for that position, and normalizing by the integration over all solid angles. Assuming that the X-Ray has an equal chance of being

emitted in any direction, then

$$P(\vec{X}) = \frac{1}{4\pi}\int_0^{2\pi} d\theta \int_0^{\pi} d\phi \sin\phi \exp[-\lambda R(\vec{X},\theta,\phi)] \tag{6.27}$$

The secondary X-Ray is emitted from the position that the incident X-Ray interacted with either a Ga or As atom through the photo-electric effect. The incident X-Ray has an equal probability of being anywhere in the y direction. The X-Ray will not, however, be equally deposited at all depths. As shown in equation (3.10), the probability of deposition of an X-Ray with a linear absorption coefficient of λ' as a function of the depth, x, is given by $\lambda' \exp(-\lambda' x)$. The probability of escape is found by integrating $P(\vec{X})$ over the area of the CCD, weighted by the probability that the secondary X-Ray originated at $\vec{X}$.

$$P(\lambda') = \frac{\int_0^{30} dx \int_0^{50} dy \exp[-\lambda' x] P(\vec{X})}{\int_0^{30} dx \int_0^{50} dy \exp[-\lambda' x]} \tag{6.28}$$

The probability of escape of secondary X-Rays from the CCD was calculated for the K_α X-Rays of Ga and As for incident X-Ray energies from Cu, Rb, Mo, Ag, Ba and Tb K_α X-Rays. The total chance for a secondary X-Ray to escape from any one event in GaAs, $\mathcal{P}$ is given by

$$\mathcal{P} = \frac{1}{2\rho_{GaAs}} (P_{Ga}\rho_{Ga}F_{Ga} + P_{As}\rho_{As}F_{As}) \tag{6.29}$$

where P_{Ga} and P_{As} are the probabilities for an escape by a K_α X-Ray from a Ga or an As atom, respectively. ρ_{GaAs}, ρ_{Ga} and ρ_{As} are the densities of GaAs, Ga and As. $F_{Ga}$and F_{As} are the fluorescence ratios of Ga and As, 50.7% and 56.2%, respectively. Table 6.8 shows the results for the calculations done for six different incident K_α X-Ray

Table 6.8: Chance of escape of the secondary X-Ray from the CCD for various incident X-Ray energies

Element	Cu	Rb	Mo	Ag	Ba	Tb
K_α X-Ray Energy (keV)[25]	8.047	13.394	17.489	22.162	32.19	44.17
Chance of escape	0.25	0.25	0.25	0.25	0.25	0.25

energies. The chance of escape is quite high, ~25% , for all the incident X-Ray energies. The insensitivity to incident X-Ray energies is because the chance of escape depends only slightly on the linear absorption coefficient of the incident X-Ray, λ'. A plot showing the effect of secondary X-Ray escape on the spectra of energies deposited into the CCD by a 44 kev X-Ray is shown in figure 6.32. The effect on the spectra of escaping secondary X-Rays is significant.

6.5.2 Escape of photo-electrons

Figure 3.9 shows the mean path length for an electron in Ge calculated using Bethe's continuous energy loss formula[32]. For a 10 keV electron in GaAs, the mean path length is 0.9 μm. The chance of escape of an electron of this energy from the detector is negligible if the electron starts more than 1 μm away from the edge of the detector. For a 50 keV electron, however, the mean path length is ~15 μm. The electron will always be within its mean path length of the edge of the detector. The chance of escape of a high energy photo-electron from the detector must therefore be taken into account when discussing the spectrum of energies deposited in the detector by an X-Ray with energy greater than

22 keV.

A Monte-Carlo simulation was done to do a more realistic study of the creation of electrons in the detector. The code used was taken from Advanced Scanning Electron Microscopy and X-Ray Microanalysis[24]. The simulation used Bethe's formula (3.13) to find the path length of the electron. The path length was then divided up into 50 equal segments, and an elastic scattering event was generated for each of these segments. The differential cross-section for elastic scattering, $d\sigma_{el}(\theta)$, was used to find the scattering angle of the electron, θ, the angle between the initial and final direction of motion of the electron. $d\sigma_{el}(\theta)$ gives the cross-section for an electron with a relativistic wavelength of λ in a solid with atomic number Z to be scattered into a solid angle $d\Omega = 2\pi \sin(\theta) d\theta$.

$$d\sigma_{el}(\theta) = \frac{\lambda^4 Z^2}{64\pi^4 a_0^2} \frac{d\Omega}{\left[\sin^2(\theta/2) + \delta\right]^2} \tag{6.30}$$

where a_0 is the Bohr radius and δ is the screening parameter which is numerically equal to

$$\delta = 3.4 \times 10^{-3} Z^{2/3}/E \quad (E \text{ in keV}) \tag{6.31}$$

λ is given by

$$\lambda = \frac{h}{(2m_0 E(1 + E/2m_0 x^2))^{1/2}} \tag{6.32}$$

where h is Planck's constant, m_0 is the rest mass of the electron and E is the energy of the electron. The probability for a scattering angle of θ is then found using 6.30 and the procedure outlined in [39].

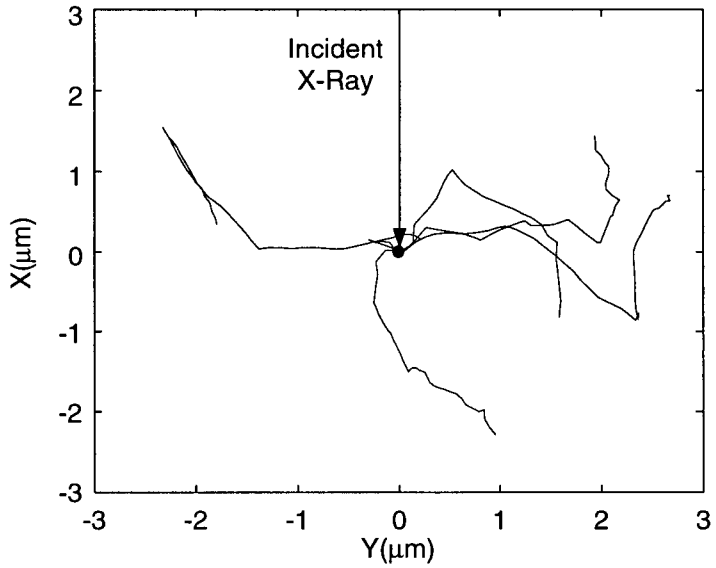

Figure 6.29: Five typical electron tracks created by the Monte Carlo simulation. The tracks were made by a 34 keV photo-electron, created by a 44 keV K_α X-Ray from Tb traveling in the negative x direction and interacting with an atom at the origin.

Figure 6.29 shows a run of 5 electron paths in Ge with an electron energy of 34 keV (the energy of the photo-electron ejected from a Ga or As atom by a Tb K_α X-Ray). The initial direction of travel of the electron was found by finding the most probable angle of ejection of the photo-electron from equation (3.12), assuming the X-Ray was incident normal to the surface of the CCD. The simulation was used to find the range of the photo-electrons, the actual distance the electron travels from its starting point. 10 000 electron paths were simulated, and the average and standard error of the range recorded. Table 6.9 shows the range, mean path length and the ratio of the range to the mean path length for electrons of various energies in Ge.

The simulation was also used to study the escape of photo-electrons from the detector

Table 6.9: Range and chance of escape of photo-electrons in Ge for various electron energies

Element	Rb	Mo	Ag	Ba	Tb	^{241}Am
K_α X-Ray energy (keV)[25]	13.394	17.489	22.162	32.19	44.17	59.54
Photo-electron energy (keV)	3.4	7.5	12.2	22.2	34.2	49.5
Mean path length (μm)	0.17	0.57	1.27	3.52	7.47	14.38
Electron range (μm)	0.047	0.161	0.394	1.231	2.85	5.97
Range/(Mean path length)	.276	.282	.310	0.35	0.38	0.42
Chance of escape	<1%	<1%	0.011	0.039	0.083	0.20

(see Table 6.9). In order to do this, the starting position of the electrons had to be chosen randomly. The deposition depth of the photons was chosen using equation (3.10), while the position in the lateral direction was equally distributed over the width of the CCD. The electrons were divided into two different populations, those that escaped from the detector and those that did not. The number of electrons that escaped was found, as well as the energy that was deposited in the detector by each escaped electron. Figure 6.30 shows a histogram of the energy deposited in the CCD by the 58390 escaped electrons created by 700 000 incident 44 keV X-rays (giving a photo-electron energy of 34 keV). The curve was fitted to an exponential rise, $F(E)$, as a function of deposited energy, E, with a rise energy of t and amplitude A

$$F(E) = A\exp(E/t) \tag{6.33}$$

The shape of the spectra from escaped photo-electrons is found by convolving a Gaussian with the distribution of energies deposited in the CCD by the escaping electrons. Figure 6.31 shows the distribution of the energies deposited by escaped electrons that

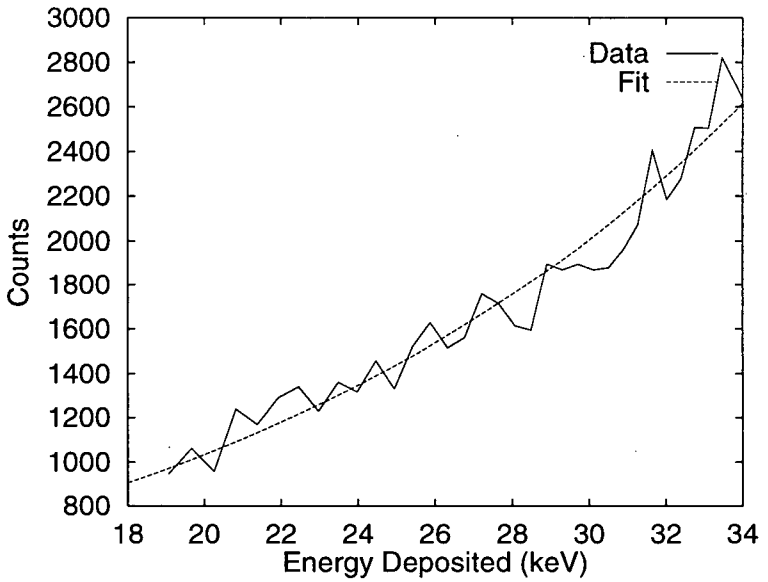

Figure 6.30: A histogram of the energy, E, deposited by a 34 keV photo-electron that escapes from the detector. A fit of Counts = 275 Exp(E/15.1 keV) was made.

would be expected for the 44 keV X-Ray from Tb. An exponential with a rise energy, t (defined in (6.33)), of 15.1 keV was convolved with a Gaussian with a half-width, σ, of 6.3 keV. The Gaussian's width was taken from the $N_{signal} = 5$ analysis of the Tb run on CCD2. Since the simulation showed that 8.3% of the photo-electrons escaped, the distribution for the energy deposited for all electrons would consist of 8.3% of the photo-escape peak plus 87.7% of the non-escape peak. The theoretical spectra for the energy deposited in the detector with and without taking the escape of photo-electrons into account is shown in figure 6.32. There is a small difference between the two cases at lower energies, but this difference is not significant compared to the statistical noise in the detector. Therefore, the escape of electrons does not appear to be a significant factor in determining the shape of the spectra in these CCDs.

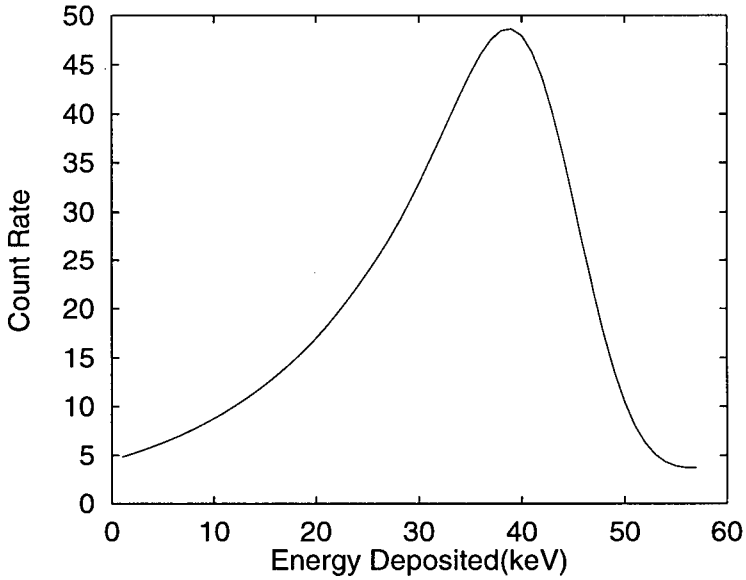

Figure 6.31: The energy deposited by a 44 keV photo-electron that escapes from the detector.

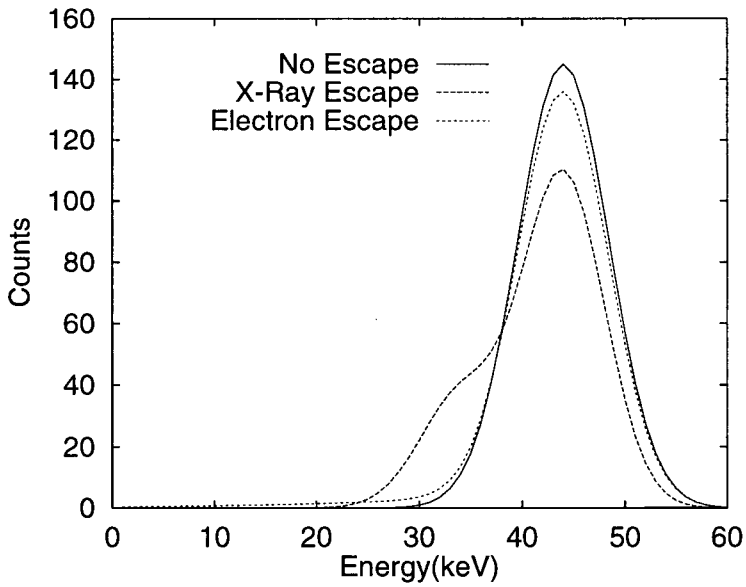

Figure 6.32: The spectrum of energies deposited in the detector for electron and secondary X-Ray escape. The incident X-Ray has an energy of 44 keV. The escape X-Ray has an energy of 10 keV, and 25% of the secondary X-Rays escape. Approximately 8% of the photo-electrons escape, and the energy deposited in the detector by them is shown in figure 6.30. See sections 6.5.1 and 6.5.2

6.5.3 Experiment

Figure 6.32 shows the theoretical spectrum for a 44 keV X-Ray for three different analyses: when no escape of particles is taken into account, when the escape of secondary X-Rays is taken into account, and when the escape of photo-electrons is taken into account. The figure shows that the escape of secondary X-rays will significantly affect the shape of the spectrum, while the escape of photo-electrons will not. Modelling the spectrum as two peaks, the signal peak and the secondary X-Ray escape peak, should result in the spectrum containing two Gaussian peaks, with the second peak 10 keV (the K_α X-Ray energy of Ga and As) lower in energy, with the same width and containing 1/3 of the events of the first.

Figure 6.33 shows the spectrum for Ba and Tb K_α X-Rays incident on CCD2. The spectrum was then fit with two Gaussians. The first Gaussian corresponding to the signal peak, and the second to the escape. The escape peak was constrained to be 10 keV below and have 1/3 the area of the signal peak. The Ba spectrum in figure 6.33-a is fit well by the escape, signal and high-energy peaks. The Tb spectrum shown in figure 6.33-b is not. Another peak had to be postulated for the Tb spectrum.

6.6 The Field-Free Peak

In order to obtain a good fit for the Tb spectra on CCD2, a third peak was postulated. The third peak was a Gaussian at lower energies than the first two, and is tentatively

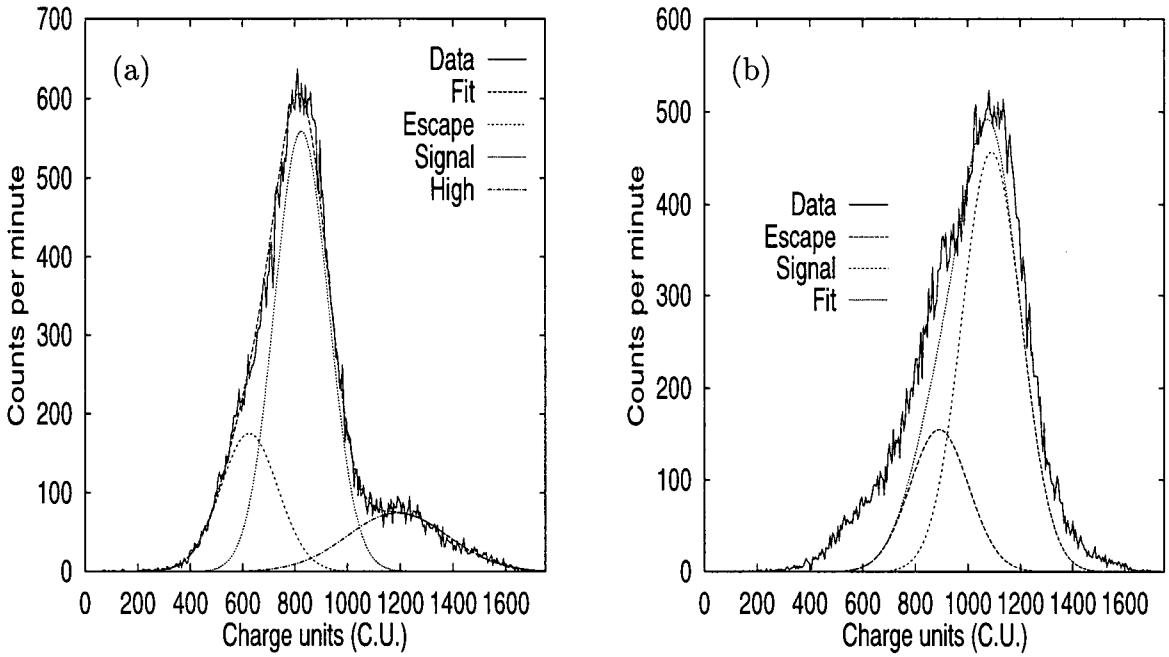

Figure 6.33: The spectra for (a)Ba and (b)Tb K_α X-Rays incident on CCD2 fit with a signal and escape peak.

identified as the field-free peak. Figure 6.34 shows the spectrum for Tb K_α X-Rays on CCD1 and CCD2 fitted with the signal, escape and field-free peaks analyzed with N_{signal} = 5. The field-free peak appears at the same position for all of the analyses of CCD2, within error (see section 5.2.1). This position is equivalent to an energy deposition in the CCD of 26 ± 3 keV.

In section 4.5, the possibility of charge that was deposited in the field-free region contributing to the spectrum was discussed. The conclusion was that this would not happen. The field-free peak hypothesis does not agree with our analysis. It is thought, instead, that photo-electron escape could account for the field-free peak. The fact that the field-free region was so large was not found until after the Monte-Carlo simulations

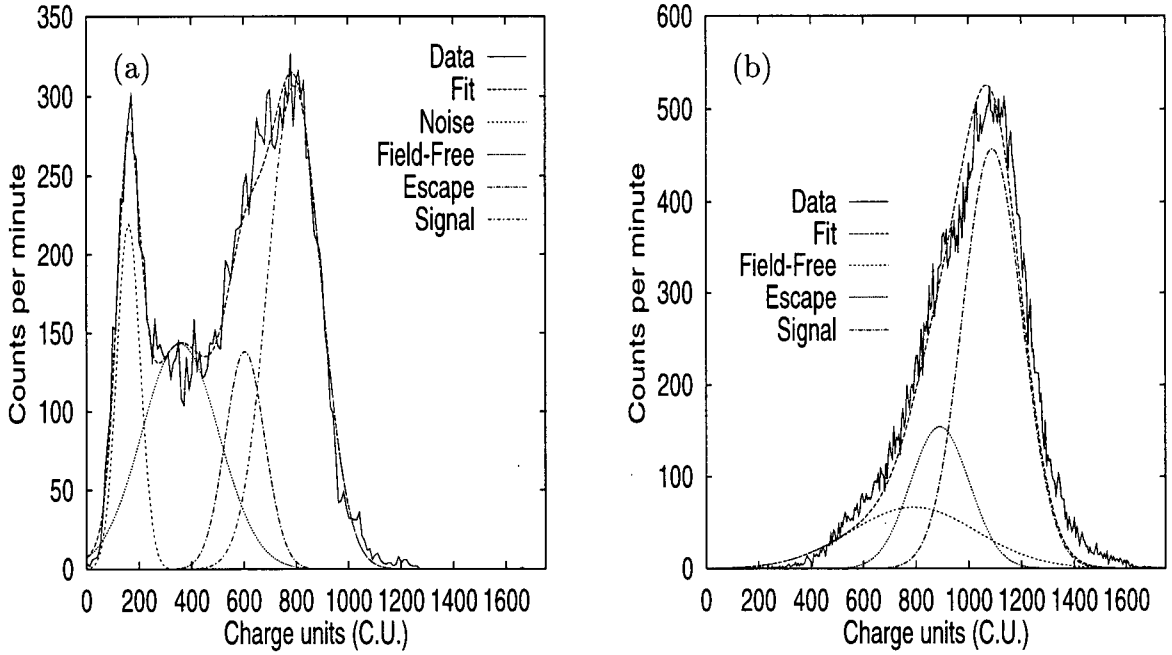

Figure 6.34: The spectrum for Tb K_α X-Rays on (a)CCD1 and (b)CCD2 analyzed with $N_{signal} = 5$ fitted with noise, signal, escape and field-free peaks.

of the photo-electron escape were made. It is possible that by redoing these simulations with an active detection area only 10 μm deep, the low energy tail created would account for the shape of the Tb spectra.

6.7 Full Spectrum Analysis

In tables 6.10 and 6.11 the positions, areas and widths for the peaks assigned to all of the spectra taken for CCD1 and CCD2 are tabulated. All of the spectra tabulated here are shown in the appendix.

Table 6.10: The peak positions (x), areas (A) and widths (w) of the peaks in the spectra from characteristic X-Rays impinging on CCD1 analyzed with $N_{signal} = 5$. The areas are in units of 1000 Charge Unit Counts, while x and w are expressed in Charge Units.

	Noise			Field Free			Escape			Signal			High Energy		
Element	A	x	w	A	x	w	A	x	w	A	x	w	A	x	w
Rb	51	172	111							101	244	72	29	782	476
Mo	68	161	99							111	312	88	6	859	436
Ag	40	207	131							48	399	100	2.3	853	355
Ba	25	200	142				14	397	105	41	577	158	9.4	873	230
Tb	26	160	89	53	357	293	26	604	150	78	794	203			

Table 6.11: The peak positions (x), areas (A) and widths (w) of the peaks in the spectra from characteristic X-Rays impinging on CCD2 analyzed with $N_{signal} = 5$. The areas are in units of 1000 Charge Unit Counts, while x and w are expressed in Charge Units. For the Cu and Rb spectra, only the High Energy 2 peak was included in the table.

	Field-Free			Escape			Signal			High Energy		
Element	A	x	w	A	x	w	A	x	w	A	x	w
Cu										98	1160	387
Rb							41	458	157	156	1169	388
Rb (run 2)							122	392	192	76	1071	509
Mo							196	551	171	33	1226	541
Ag							213	614	176	14	1227	450
Ba				48	625	220	14	825	206	35	1189	381
Ba (run 2)				48	632	214	142	836	200	32	1195	335
Tb	40	790	481	43	891	222	120	1091	226			
Tb (run 2)	20	619	232	51	858	187	153	1102	245			

6.8 The ^{241}Am Spectrum

6.8.1 Theory

^{241}Am emits both α-particles and X-Rays. The ^{241}Am source used in this study was shielded so that the α-particles would be absorbed, but the X-Rays would emerge unimpeded. Because the source emits a large number of X-Rays at different energies and intensities, the spectrum for ^{241}Am had to be calculated. The energies and probabilities of each different X-Ray transition of ^{241}Am are shown in table 6.12[25]. Also shown in this table are the linear absorption coefficients of each of those X-Rays in GaAs. The linear absorption coefficients were then used to calculate the probability that each of the X-Ray energies would be absorbed in 30 μm of GaAs, using equation (3.10). The probability of absorption was then multiplied by the probability of an emission of that energy from the ^{241}Am source to get the probability of an event in the CCD at that energy.

Using the results shown in Table 6.12, the spectrum of ^{241}Am was calculated. For each energy there was a Gaussian distribution with a fixed width and an area given by the probability of an event from that energy. The Gaussians were then added, and the result called the theoretical ^{241}Am spectrum (see figure 6.35). Significant peaks are expected at 13.9, 18.6 and 59.5 keV. This spectrum does not take into account any escape of secondary X-Rays or photoelectrons, but gives an idea of what the spectrum should look like.

Table 6.12: X-Rays emitted by ^{241}Am , and their probability of absorption in 30μm of GaAs. Multiplying these two probabilities give the probability that an event from this energy of X-Ray will be seen in the CCD.

X-Ray energy (keV)	Probability of emission from ^{241}Am	linear absorption coefficient (1/cm)	probability of absorption in 30 μm of GaAs	probability of event from this energy
11.871	0.81	886.22	.930	0.028
13.927	13	586.96	.828	0.399
15.861	0.33	416.68	.714	0.009
18.611	20.2	270.2	.555	0.416
20.977	5.2	194.62	.442	0.085
26.345	2.4	103.01	.266	0.024
33.192	0.12	53.61	.149	0.001
59.5364	35.7	9.76	.029	0.038

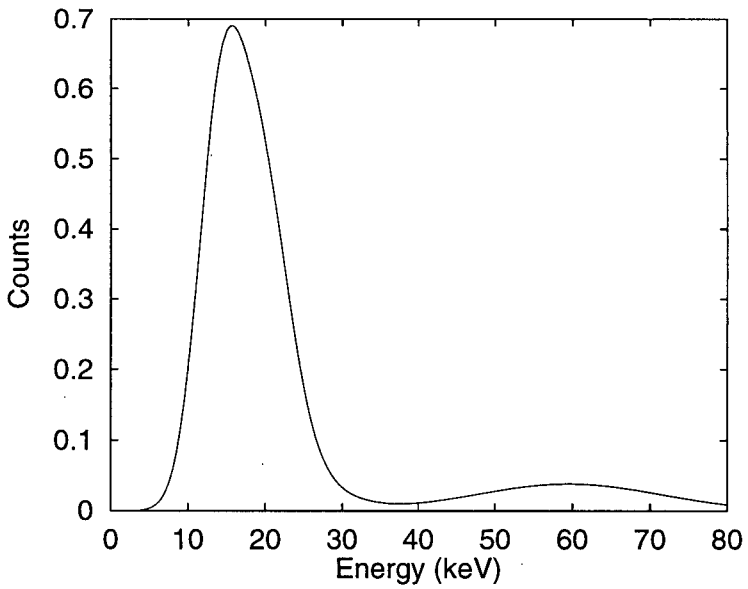

Figure 6.35: Theoretical ^{241}Am spectrum in 30 μm of GaAs

Table 6.13: Peak data for the ^{241}Am X-Rays on CCD2 analyzed with $N_{signal} = 5$. The x-axis was calibrated using the CCD2 5 peak calibration. The areas are in units of keV Counts, while x and w are expressed in keV.

Peak Name	A (keV Counts)	x (keV)	w (keV)
13 keV	4201	13.1	6.1
18 keV	4450	17.9	12.1
Field Free	5631	43.5	16.0
Escape	906	45.8	7.1
60 keV	2719	55.6	8.0

6.8.2 Experiment

Figure 6.36 shows the data obtained from shining an ^{241}Am source on the top of CCD2. The $N_{signal} = 5$ data was fit with five Gaussian peaks, each of them corresponding to an expected peak. The peaks were the 13 keV, 18 keV, 60 keV and the escape and field-free peaks corresponding to the 60 keV peak. The fit of the escape peak was constrained to be 10 keV below the 60 keV peak and have one third the area. The results of this are shown in figure 6.36 and table 6.13. The resulting fit shows the 13 keV and 18 keV peaks to be where they were expected, and the 60 keV peak to be centred at 57 keV on the calibration scale. The ratio of the areas of the 60 keV peak to the 13 and 18 keV peaks is much larger than predicted in Section 6.8.1. The resolution of the CCD at 60 keV is 9.6 keV FWHM. Table 6.14 shows a comparison of this resolution to some other studies using single element GaAs detectors.

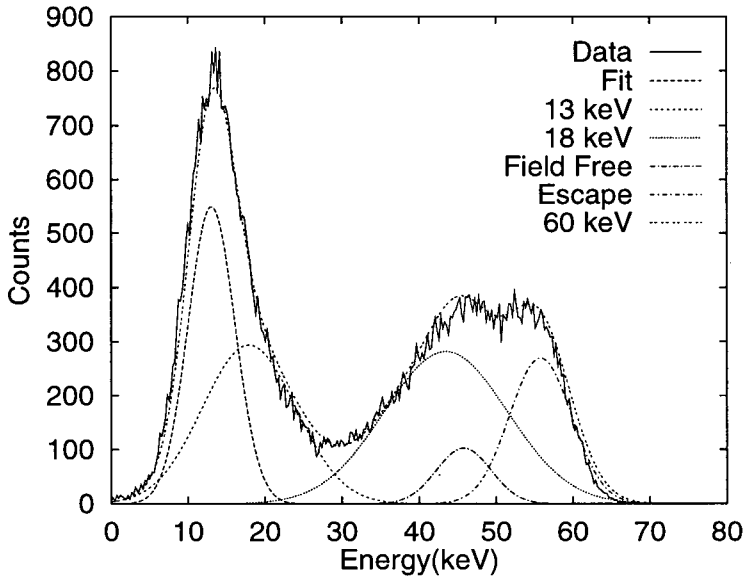

Figure 6.36: The spectrum of ^{241}Am on CCD2 fit with five peaks: The 13 keV, 18 keV and 60 keV peak and the escape and field-free peaks corresponding to the 60 keV peak.

Table 6.14: Comparison of the GaAs CCD X-Ray detector's resolution at 60 keV to some other GaAs detectors.

Authors	Detector Type	Temperature(°C)	FWHM[%]	FWHM[keV]
Holland et. al.[40]	LEC GaAs	-10	7.5	4.5
McGregor et. al.[41]	LEC GaAs	R.T.	37	22
Bencivelli et. al.[42]	LEC GaAs	R.T.	7.5	4.5
Bertuccio et. al.[15]	LEC GaAs	20	28	16.8
Bertuccio et. al.[15]	LEC GaAs	-30	3.7	2.2
Hesse et. al. [43]	epitaxial GaAs	R.T.	4.3	2.6
This Work	GaAs CCD	R.T.	16	9.6

Table 6.15: Range in the x-direction and chance of charge sharing for photoelectrons in Ge

Element	Ba	Tb	^{241}Am
K_α X-Ray energy (keV)	32.19	44.17	59.54
Photo-electron energy (keV)	22.2	34.2	49.5
range of the electron in the X-direction, l (μm)	0.682	2.86	3.08
Chance for charge sharing	0.035	0.075	0.15

6.9 Charge Sharing

The Monte Carlo simulation was also used to examine charge sharing in the CCD (see section 4.4). The extent of the initial photo-electron's track in the x-direction was found. The chance of charge sharing, $P(x)$, for a track with an extent in the x-direction of l microns in a CCD with an anode pitch of A is given by $P(l) = l/A$. The chance of charge sharing for X-rays of 59 keV, 44 keV and 32 keV was calculated. The average range in the x-direction and the chance for charge sharing for these three energies are shown in table 6.15. Because the photo-electron's path length is always less than the pixel spacing (20 μm), there is essentially no chance of charge sharing into more than two pixels.

The fact that a value of N_{signal} of 5 had to be used for the Tb and higher energy spectra shows that some charge sharing occured. This could be caused by charge "spilling" from one pixel into another, as discussed in section 4.4.

Chapter 7

Conclusion

7.1 Future Work

There are a number of possibilities for further research and development of the CCD X-Ray detector. These possibilities include methods for increasing the resolution of the detector, better characterizing the detector, and increasing the types of particles studied. The top priority should, however, be an analysis of the sources of noise in the device. One likely source is the output circuitry on the CCDs used in the study. The output circuitry on the CCDs used for the BNL 787 experiment has been greatly improved since the two wafers of CCDs used for this study were fabricated. A second fabrication using this improved output circuitry should greatly reduce the noise of the baseline of the CCD. A second method of increasing the resolution may be to cool the CCD. A study[15] using a bulk LEC grown GaAs detector detected the 60 keV ^{241}Am X-Ray with a resolution of 28% at 20°C. By cooling the detector to -30°C, the resolution was increased to 3.6%. Further increases in resolution might also be obtained by characterizing individual pixels of the CCD. If it was known which pixel an X-Ray deposited charge into, then the known characteristics of that pixel could be used to further reduce the variance of the charge

read out.

A further study of the field-free region would also be useful. Knowledge of the true depth of the depletion region would allow a proper analysis of the effect of the escape of photo-electrons on the shape of the spectra for Tb X-Rays through further Monte Carlo simulations. This knowledge would further test the assignation of the field-free peak to the escape of photo-electrons from the depletion region. Holland et. al.[40] suggest that measuring the count rate of 60 keV ^{241}Am X-Rays as a function of bias would give a measure of the depth of the actual depletion region.

Another possible direction for future research would be to increase the depth of the depletion region. This should allow a greater detection efficiency and should also lower the relative intensities of the field-free and escape peaks. In order to increase the depth of the field-free region without increasing the bias voltage, the purity of the intrinsic GaAs would have to be increased. The depth of the depletion region is inversely proportional to the square root of the doping density in the active region. If the intrinsic doping density was decreased from 10^{14} cm^{-3} to 10^{13} cm^{-3}, the active region would be fully depleted at a bias voltage of 7 V.

The ability of the CCD detector to detect X-Rays also implies that it should be able to detect other particles. A minimum ionizing particle in GaAs will lose energy at a rate of $dE/dx = 5.6$ MeV/cm[44]. In 30 μm, a minimum ionizing particle will deposit 16.8 keV, or 4000 e.h.p.s, in the CCD, roughly equivalent to the 17.5 keV deposited by a Mo K_α X-Ray. This number of e.h.p.s is detected by the detector, implying that electrons

and α rays will be seen by the detector. Detectors used for detecting minimum ionizing particles would be much more useful if they could also be used to detect the position and direction of travel of the particles. In order to detect position, the pixel that the charge was deposited into by the particle would have to be known. The direction of travel of the particle could be found by finding the position of the particle as it traveled through several detectors. In order for this to be feasible, the energy lost by the particle as it traversed each detector would have to be low. In the detector as it is now, a minimum ionizing particle will lose ~350 keV in the LEC substrate of the detector. This could be lowered if the substrate was made thinner than its current 650 μm.

7.2 Conclusions

The response of a buried channel GaAs CCD detector to X-Rays ranging in energy from 8 to 60 keV was studied. The spectra from single-energy X-Ray sources were not simple Gaussians, but generally contained a number of different peaks. Five different peak types, the noise, signal, escape, high-energy and field-free peaks, were identified. The mechanisms for their creation have been either established or tentatively assigned.

The noise peak results from triggers due to noise in the CCD waveform rather than X-Ray caused events. The signal peak is the expected peak resulting from full deposition of the X-Ray's energy in the detector. The position of the signal peak was found to be linear as a function of incident X-Ray energy for X-Ray energies ranging from 14 keV to 44 keV. The resolution of the detector varied from 57% at 14 keV to 16% at 60 keV. The

escape peak results from the escape of secondary X-Rays from the detector. Simulations were made to estimate the relative intensity of the escape peak to the signal peak. This intensity was then used to make fits to the experimental spectra. The high-energy peak was found to be constant in energy and shape for all the K_α spectra with an energy of 50 keV. Its origin has been tentatively assigned to an X-Ray event caused by back-scattered 60 keV ^{241}Am X-Rays leaked from the source. The field-free peak is believed to result from the escape of photo-electrons from the depletion region.

The resolution of the detector is larger (worse) than that of other single element GaAs X-Ray detectors, but it is believed that improvements in the resolution can be made, as outlined in section 7.1. These studies showed that X-Rays were detectable, and that the energy deposited in the CCD by a minimum ionizing particle would be detectable by the CCD.

Bibliography

[1] W.S. Boyle and G.E. Smith "Charge Coupled Semiconductor Devices" *Bell Systems Technical Journal* **49** (1970) 587.

[2] G.F. Amelio "Experimental Verification of the CCD Concept" *Bell Systems Technical Journal* **49** (1970) 593.

[3] A.R. Walker "BVI CCD astronomy of galactic globular clusters. II. M68" *Astronomical Journal*, **108** (1994) 555.

[4] C.S. Barth et. al. "CCD imaging of NGC 4861:ionized gas properties and stellar formation" *Astronomical Journal* **108** (1994) 2069.

[5] C.S. Burley et. al. "A precisely aligned CCD mosaic" *Astronomical Society of the Pacific* **108** (1994) 1024.

[6] W.P. Acker et. al. "The use of a charge-coupled device and position sensitive anode detector for multi-order spontaneous Raman spectroscopy from Silicon" *JAP* **64** (1988) 2263.

[7] M.H. Abd-el-Barr and Z.G. Vranesic "Charge coupled device implementation of multi-valued logic systems" *IEE Proc. E Computers and Digital Techniques* **136** (1989) 306.

[8] A.H. Baher "Design of finite duration impulse response digital and charge coupled device filters with arbitrary attenuation characteristics" *IEE Proc. G Electronic Circuits and Systems* **132** (1985) 193.

[9] R. Hayes and D.L. Heidtman "Dual channel charge coupled device for high speed signal acquisition" *Optical Engineering* **26** (1987) 829.

[10] A.J. Holland et. al. "The X-Ray polarization sensitivity of CCDs" *Nucl. Instr. and Meth.* **A 355** (1995) 526.

[11] K.J. McCarthy et. al. "Modeling the X-Ray response of charge coupled devices" *Nucl. Instr. and Meth.* **A 362** (1995) 538.

[12] K.J. McCarthy and A. Wells, Proc 10th Symp. on Photo-electric Imaging Devices, Institute of Physics Conference Series 121 (1992) 17.

[13] E. Bertolucci et. al. "X-ray imaging using a pixel GaAs detector" *Nucl. Instr. and Meth.* **A 362** (1995) 547.

[14] L. Berlutti et. al. "Gallium Arsenide particle detectors: a study of the active region and charge-collection efficiency" *Nucl. Instr. and Meth.* **A 354** (1995) 364.

[15] G. Bertuccio et. al. "Performance of SI LEC GaAs detectors at 20°C and -30°C for X- and γ-ray spectroscopy" *Nucl. Instr. and Meth.* **A 379** (1996) 152.

[16] R. Bertin et. al. "A preliminary study of GaAs solid state detectors for high energy physics" *Nucl. Instr. and Meth.* **A 294** (1990) 211.

[17] S.P. Beaumont et. al. "GaAs solid state detectors for particle physics" *Nucl. Instr. and Meth.* **A 322** (1992) 472.

[18] K.M. Smith "GaAs detector performance and radiation hardness" *Nucl. Instr. and Meth.* **A 368** (1995) 220.

[19] D.A. Bryman et. al. "500 MHz transient digitizers based on GaAs CCDs" submitted to *Nucl. Instr. and Meth.*

[20] J.-I. Song et. al. "GaAs CCD readout for engineered bandgap detectors" *Proc. SPIE* **1308** (1990) 254.

[21] S.M. Sze, Physics of Semiconductor Devices, 2nd edition. John Wiley (Toronto) 1981.

[22] M.S. Tyagi "Physics of Schottky barrier junctions" in *Metal Semiconductor Schottky Barrier Junctions and Their Applications* (B.L. sharma, ed.) Plenum (New York) 1984.

[23] D.E. Newbury in *SEM Microcharacterization of Semiconductors* (D.B. Holt and D.C. Joy, eds) Academic Press, (Toronto) 1989.

[24] D.E. Newbury "Modeling Electron Beam-Specimen Interactions" in *Advanced Scanning Electron Microscopy and X-Ray Microanalysis* (D.E. Newbury, ed) Plenum, (New York) 1986.

[25] N.G. Gusev and P.P. Dmitrev, *Quantum Radiation of Radioactive Nuclides*, Pergammon (New York) 1979.

[26] H. He et. al, "A detailed study of the interaction mechanisms for Si(Li) detector response functions by the direct Monte Carlo approach" *Nucl. Instr. and Meth.* **A 272** (1988) 847.

[27] Condon and Odishaw, *Handbook of physics*, 2nd edition. McGraw-Hill (New York) 1967.

[28] E.J. McGuire "Auger and Coster-Kronig Transitions" in *Atomic Inner Shell Processes, B Vol 1* (B. Crasemann, ed.) (1975) 293–330.

[29] M.O. Krause "Atomic radiative and radiationless yields for K and L shells" *J. Phys. Chem. Ref. Data.* **8** (1979) 307.

[30] J.L. Blakenship and W.F. Mruk *Bull. Amer. Phys. Soc.* **9** (1964) 49.

[31] J.E. Eberhardt et. al. "Evaluation of epitaxial n-GAs for nuclear radiation detection" *Nucl. Instr. and Meth.* **94** (1971) 463.

[32] H.A. Bethe and J. Ashkin in *Experimental Nuclear Physics*, Vol 1 (E Segrè, ed) John Wiley, (New York) 1953.

[33] J. Shah et. al., "Determination of intervalley scattering rates in GaAs by subpicosecond luminescence spectroscopy", *Phys. Rev. Lett.* **59** (1987) 2222.

[34] R.P. Gardner et. al. "An investigation of the possible interaction mechanisms for Si(Li) and Ge detector response functions by Monte Carlo simulation" *Nucl. Instr. and Meth.* **A 242** (1986) 399.

[35] G.C. Messenger, "Collection of charge on junction nodes from ion tracks", *IEEE TNS*, **NS-29** (1982) 2024.

[36] M. Shur et. al., "Charge collection by drift during single particle upset", *IEEE TNS*, **NS-33** (1986) 1140.

[37] J.G. Ruth and G.S. Kino "Measurement of the velocity field characteristic of Gallium Arsenide" *Appl. Phys. Lett.* **10** 40.

[38] R.J. Nelson and R.G. Sobers "Minority carrier lifetime and internal quantum efficiency of surface-free GaAs" *J. Appl. Phys.* **49** (1978) 6103.

[39] L. Reimer, *Scanning Electron Microscopy*, Springer-Verlag, (Berlin) 1985.

[40] A.D. Holland et. al. "X-Ray detection using bulk GaAs" *Nucl. Instr. and Meth.* **A 346** (1994) 366.

[41] D.S. McGregor et. al. "Bulk GaAs room temperature radiation detectors" *Nucl. Instr. and Meth.* **A 322** (1992) 487.

[42] W. Bencivelli et. al. "Some new results on semi-insulation GaAs detectors for low energy X-rays" *Nucl. Instr. and Meth.* **A 355** (1995) 425.

[43] K. Hesse et. al. "Room-Temperature GaAs gamma detectors" *Nucl. Instr. and Meth.* **101** (1972) 39.

[44] H. Esbensen et. al. "Random and channeled energy loss in thin Germanium and Silicon crystals for positive and negative 2–15 GeV/c pions, kaons and protons" *Phys. Rev. B* **18** (1978) 1039.

Chapter 8

Appendix: Spectra

All of the single-energy spectra taken during this study are reproduced here with all curve fits. The areas, widths and positions of the peaks shown in the spectra are tabulated in tables 6.10 and 6.11.

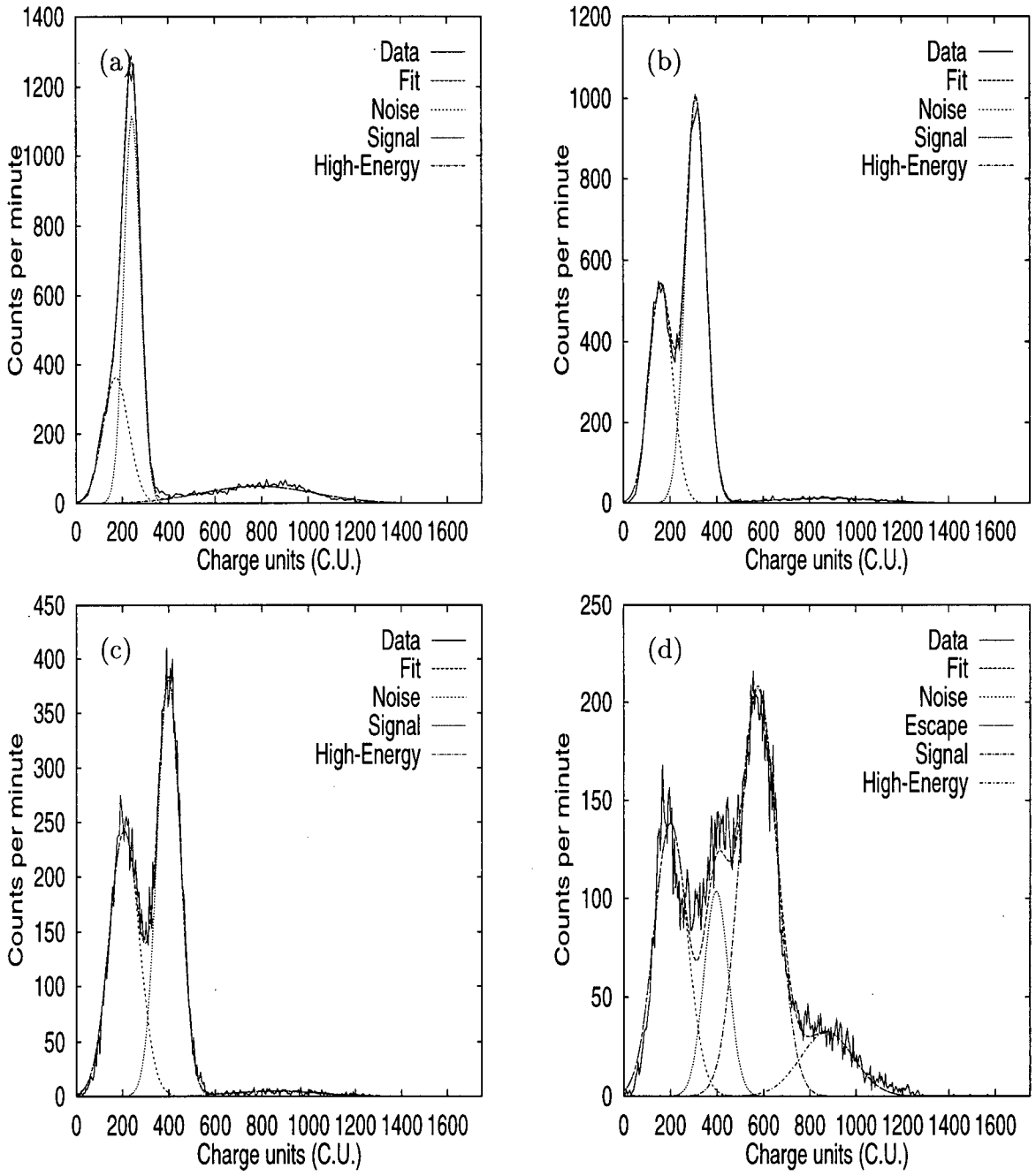

Figure 8.37: Spectra for X-rays impinging on CCD1 analyzed with $N_{signal} = 5$ for the characteristic X-Rays of (a)Rb, (b)Mo, (c)Ag and (d)Ba.

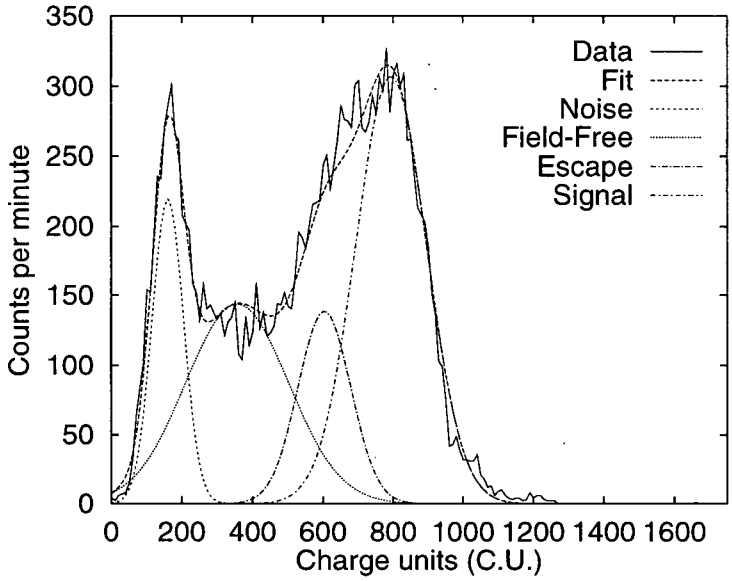

Figure 8.38: Spectra for X-rays impinging on CCD1 analyzed with $N_{signal} = 5$ for the characteristic X-Rays of Tb

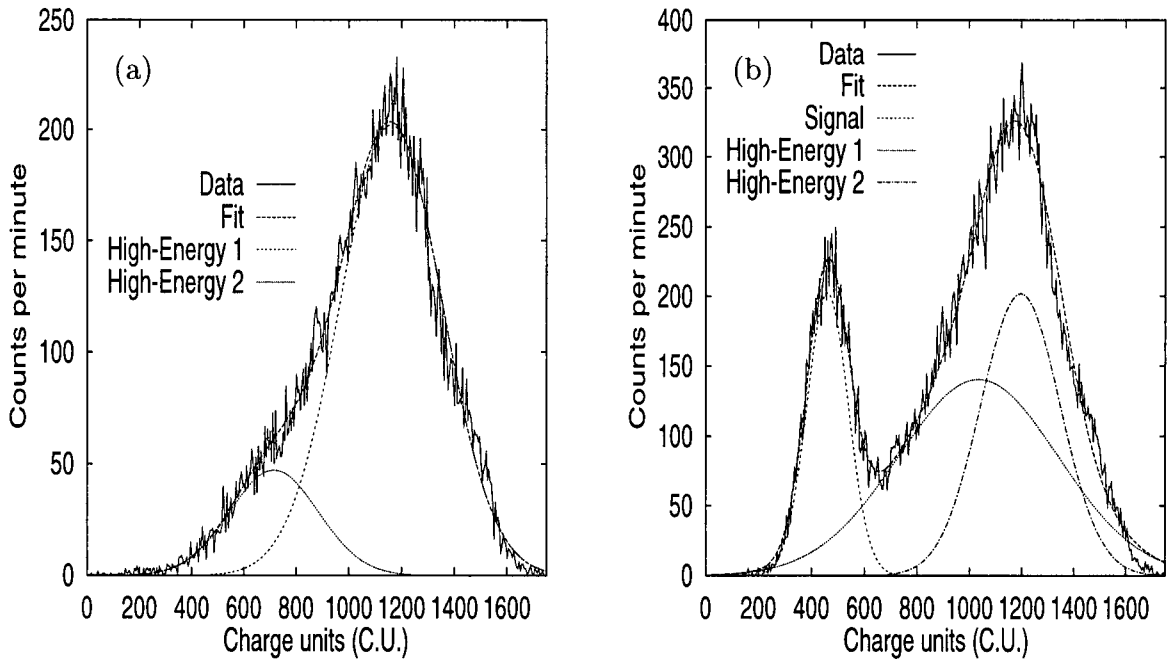

Figure 8.39: Spectra for X-rays impinging in CCD2 analyzed with $N_{signal} = 5$ for the characteristic X-Rays of (a)Cu and (b)Rb.

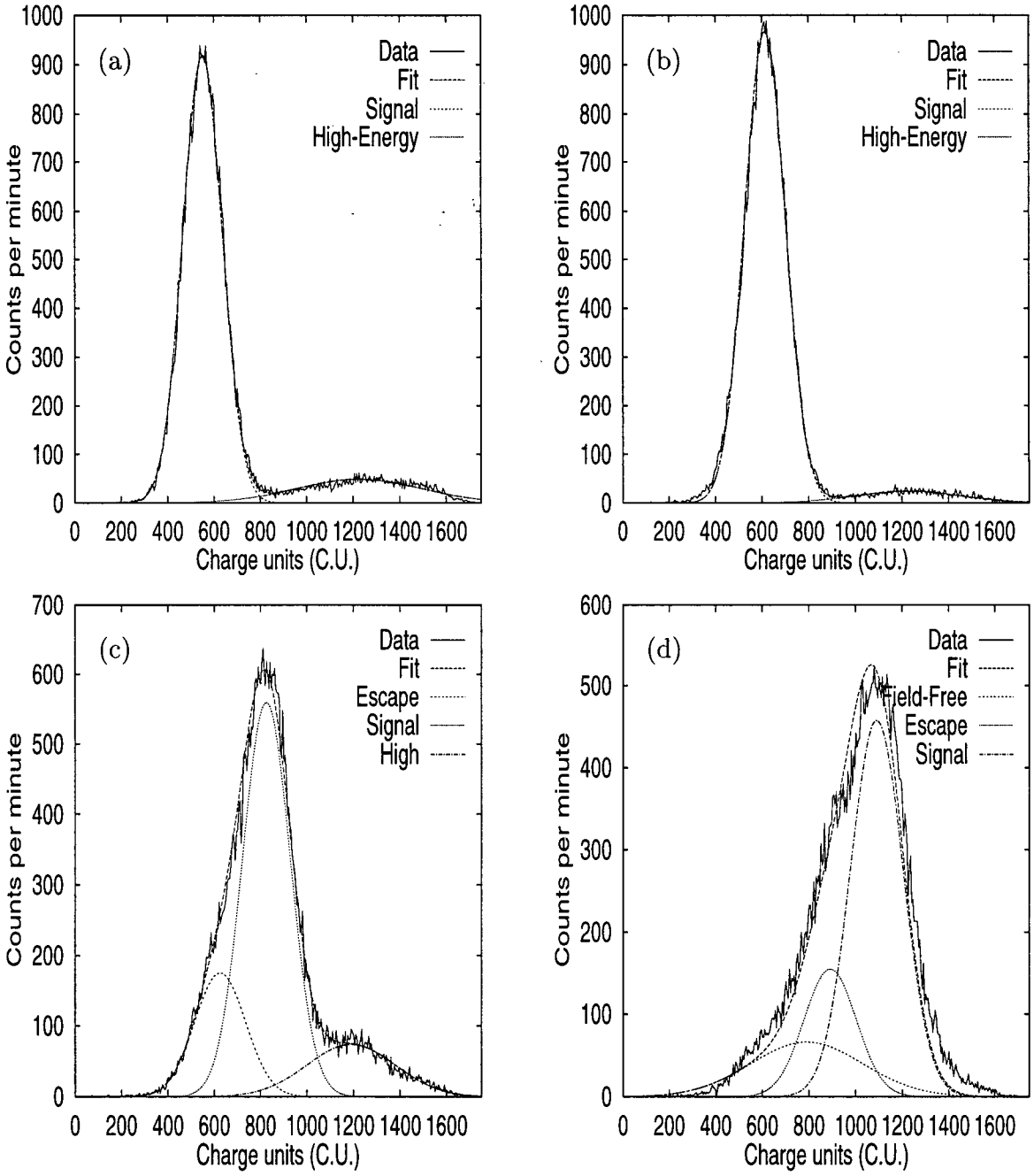

Figure 8.40: Spectra for X-rays impinging on CCD2 analyzed with $N_{signal} = 5$ for the characteristic X-Rays of (a)Mo, (b)Ag, (c)Ba and (d)Tb.

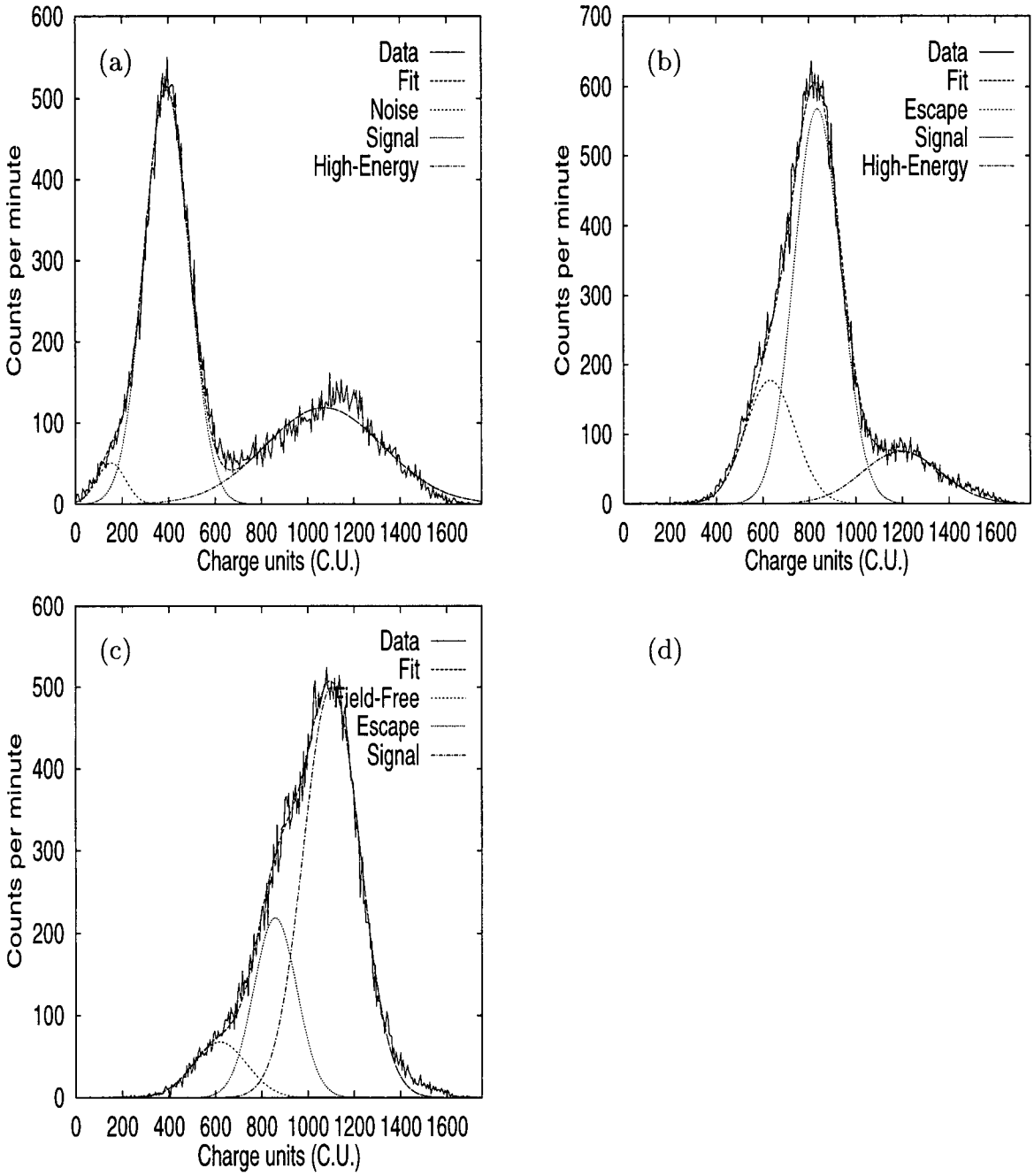

Figure 8.41: Spectra for a second set of X-Rays impinging on CCD2 analyzed with N_{signal} = 5 for the characteristic X-Rays of (a)Rb, (b)Ba and (c)Tb.